

Probing Reionization and Early Cosmic Enrichment with the Mg II Forest

Joseph F. Hennawi,¹^{*} Frederick B. Davies,^{1,2} Feige Wang,^{1,3,*} and Jose Oñorbe⁴

¹ Department of Physics, Broida Hall, University of California, Santa Barbara Santa Barbara, CA 93106-9530, USA

² Lawrence Berkeley National Laboratory, CA 94720-8139, USA

³ Steward Observatory, University of Arizona, 933 North Cherry Avenue, Tucson, AZ 85721, USA

* NHFP Hubble Fellow

⁴ Facultad de Físicas, Universidad de Sevilla, Avda. Reina Mercedes s/n, Campus de Reina Mercedes, 41012 Sevilla, Spain

Accepted XXX. Received YYY; in original form ZZZ

ABSTRACT

Because the same massive stars that reionized the intergalactic medium (IGM) inevitably exploded as supernovae that polluted the Universe with metals, the history of cosmic reionization and enrichment are intimately intertwined. While the overly sensitive Ly α transition completely saturates in a neutral IGM, strong low-ionization metal lines like the Mg II λ 2796, λ 2804 doublet will give rise to a detectable ‘metal-line forest’ if the metals produced during reionization ($Z \sim 10^{-3} Z_{\odot}$) permeate the neutral IGM. We simulate the Mg II forest for the first time by combining a large hydrodynamical simulation with a semi-numerical reionization topology, assuming a simple enrichment model where the IGM is uniformly suffused with metals. In contrast to the traditional approach of identifying discrete absorbers, we treat the absorption as a continuous random field and measure its two-point correlation function, leveraging techniques from precision cosmology. We show that a realistic mock dataset of 10 JWST spectra can simultaneously determine the Mg abundance, [Mg/H], with a 1σ precision of 0.02 dex and measure the global neutral fraction $\langle x_{\text{H I}} \rangle$ to 5% for a Universe with $\langle x_{\text{H I}} \rangle = 0.74$ and [Mg/H] = -3.7 . Alternatively, if the IGM is pristine, a null-detection of the Mg II forest would set a stringent upper limit on the IGM metallicity of [Mg/H] < -4.4 at 95% credibility, assuming $\langle x_{\text{H I}} \rangle > 0.5$ from another probe. Concentrations of metals in the circumgalactic environs of galaxies can significantly contaminate the IGM signal, but we demonstrate how these discrete absorbers can be easily identified and masked such that their impact on the correlation function is negligible. The Mg II forest thus has tremendous potential to precisely constrain the reionization and enrichment history of the Universe.

Key words: cosmology: theory - dark ages - reionization - first stars - galaxies: high-redshift - intergalactic medium - quasars: absorption lines - methods: numerical.

1 INTRODUCTION

The process of converting primordial hydrogen and helium into heavier elements underlies the entire history of star and galaxy formation in the Universe. During the Epoch of Reionization (EoR) primeval galaxies and accreting black holes ionized the hydrogen in the intergalactic medium (IGM) ending the preceding cosmic ‘dark ages’. Current Planck constraints suggest reionization took place in the range $z_{\text{reion}} \approx 5.9 - 8.0$ (2σ ; Planck et al. 2018), consistent with other astrophysical constraints from IGM damping

wings towards the highest redshift quasars (Mortlock et al. 2011; Greig et al. 2017; Bañados et al. 2018; Davies et al. 2018b; Greig et al. 2019; Wang et al. 2020; Yang et al. 2020) and the disappearance of strong Ly α emission from galaxies (Mason et al. 2018, 2019; Hoag et al. 2019). In the same way that the reionization history provides a global census of ionizing photons emitted by all galaxies and quasars, the metal content of the IGM provides a fossil record of the Universe’s integrated star-formation history. Indeed, the production of ionizing photons and metals go hand-in-hand because the same massive stars emitting the ionizing photons explode as supernovae ejecting metals into their surroundings. Considerations based solely on the lifetimes and yields of massive

* E-mail: joe@physics.ucsb.edu (JFH)

stars generically predict that in the process of producing the ≈ 3 photons per hydrogen atom required to reionize the Universe the average metallicity will reach $Z \sim 10^{-3} Z_{\odot}$ (Madau & Shull 1996; Miralda-Escudé & Rees 1997; Gnedin & Ostriker 1997; Ferrara 2016), largely insensitive to the shape of the stellar IMF.

While the inevitable production of these metals at early times is uncontroversial, their abundance, distribution, and ionization state are far less clear. Models can be found where the pre-reionization IGM is polluted to $Z \sim 10^{-3} Z_{\odot}$ already at $z \sim 8-9$ (Madau et al. 2001; Pallottini et al. 2014; Jaacks et al. 2018, 2019; Doughty & Finlator 2019; Kirihara et al. 2020), possibly explaining the background metallicity of the IGM measured at $z \approx 3$ (Schaye et al. 2003); whereas in other studies metals remain highly concentrated around the galaxies producing them (Oppenheimer et al. 2009; Pawlik et al. 2017) while the IGM remains pristine. There is even less consensus about whether these enriched regions are necessarily simultaneously reionized, either by ionization fronts from the galaxies responsible for the pollution, or the ‘enrichment-front’ powered by galactic outflows, which can shock heat and collisionally ionize the gas (Madau et al. 2001; Ferrara 2016). Alternatively, neutral enriched material could exist in the pre-reionization IGM if it recombines due to the stochasticity of reionization (Oh 2002), or if galactic outflows were not fast enough to collisionally ionize it, or if these outflows do not open up the necessary channels for ionizing photons to penetrate outflowing enriched gas.

Metal absorption lines at the highest redshifts provide an additional window into the physics of reionization. At $z \lesssim 5$ after reionization is complete, heavy elements are ubiquitously detected in the IGM as extremely weak absorption in high-ionization states like C IV and O VI (e.g. Ellison et al. 2000; Bergeron et al. 2002; Simcoe 2011; D’Odorico et al. 2016), owing to low IGM densities $n_{\text{H}} \sim 10^{-5} - 10^{-4} \text{ cm}^{-3}$ and the relatively hard UV background. The smoking gun of reionization as probed by metal absorbers would be a transition from these weak high-ionization lines to a forest of low-ionization absorbers from transitions like O I $\lambda 1302 \text{ \AA}$, Si II $\lambda 1260 \text{ \AA}$, C II $\lambda 1334 \text{ \AA}$, and Mg II $\lambda 2796 \text{ \AA}, \lambda 2804 \text{ \AA}$ as the IGM becomes progressively more neutral (Oh 2002), provided the pre-reionization IGM is sufficiently enriched.

To date all of our knowledge of the so-called background metallicity of the IGM comes from $z \sim 2-4$, where the sensitive high-resolution and high S/N ratio ($\sim 50-200$) echelle absorption line spectra required to measure this quantity are easiest to obtain. This work has revealed that the IGM is enriched to a level $Z \approx 10^{-3} Z_{\odot}$ at $z \sim 2-4$ (Ellison et al. 2000; Bergeron et al. 2002; Schaye et al. 2003; Aguirre et al. 2004, 2008; Simcoe 2011) down to as low as the cosmic mean density, indicating that $> 50\%$ of the baryonic mass in the universe has been polluted with metals (Booth et al. 2012; D’Odorico et al. 2016). Interestingly, Schaye et al. (2003) found no evidence for evolution over the redshift range $1.8 < z < 4.1$, during which the cosmic star-formation decreases by ~ 0.5 dex, suggesting that a significant amount of the IGM enrichment could have occurred at early times. The highest redshift IGM metallicity measurement comes from Simcoe (2011) who measured C/H ≈ -3.55 at $z \sim 4.3$, and argued for a mild (0.3–0.5 dex) decrease from $z \sim 2.4$. Whether this decrease is at odds with the lack of evolution observed by Schaye et al. (2003) is unclear, and as empha-

sized by Simcoe (2011) could partly result from methodological differences between the Schaye et al. (2003) pixel optical depth technique and Simcoe (2011)’s traditional Voigt profile fitting approach.

Notwithstanding significant observational efforts, it has proven too difficult to detect the extremely weak absorption lines that would herald the transition to a neutral IGM at $5 \lesssim z \lesssim 7$ because the relevant transitions are redshifted into the near-IR. Due to the higher sky background, increased detector noise, lower resolution spectrographs, and exacerbated by the paucity of sufficiently bright high-redshift quasars, the resulting spectra lack the required sensitivity to probe the diffuse IGM. For example, the vast majority of $z > 5$ CIV detections published in the literature to date have $N_{\text{CIV}} > 14 \text{ cm}^{-2}$ – a direct result of the limiting column densities (i.e. 50% completeness) of the respective surveys (Ryan-Weber et al. 2009; Becker et al. 2009; Simcoe et al. 2011; D’Odorico et al. 2013). For comparison, at $z \approx 6$ if the IGM has a metallicity of $Z = 10^{-3.5} Z_{\odot}$ a CIV absorber arising from gas at the cosmic mean density would have¹ $N_{\text{CIV}} = 10^{11.8} \text{ cm}^{-2}$. This implies current $z \gtrsim 5$ CIV searches are probing overdense ($\rho/\langle\rho\rangle \sim 100$) gas in the circumgalactic medium (CGM) of galaxies which is at much higher metallicity than the background IGM. Similarly, the majority of the O I absorbers published by recent surveys (Becker et al. 2006, 2011, 2019) have $N_{\text{OI}} > 10^{14} \text{ cm}^{-2}$ corresponding to rest-frame equivalent widths of $W_{\lambda} \gtrsim 0.1 \text{ \AA}$, whereas the hydrodynamical simulations performed by Keating et al. (2014) demonstrate that such absorbers arise from CGM gas at overdensities of $\rho/\langle\rho\rangle \gtrsim 80$ characteristic of so-called subdamped Ly α systems. This is in line with the conclusions of Simcoe et al. (2012)’s search for a forest of Mg II absorbers in the neutral region surrounding a quasar at $z \approx 7$ – with current sensitivity only significantly overdense or chemically enriched absorbers would be detectable as discrete lines, but the diffuse IGM at metallicity [Mg/H] < -3 is presently beyond reach. Thus, for both high and low-ions, current metal absorption line searches probing into the EoR can only individually identify the strongest absorbers arising from dense gas in the CGM of galaxies.

It has been observed that the cosmic mass density of CIV absorbers Ω_{CIV} drops by a factor of ~ 2 at $z > 5.3$ (Ryan-Weber et al. 2009; Becker et al. 2009; Simcoe et al. 2011; D’Odorico et al. 2013), at around the same redshift that an upturn in the abundance of O I absorbers is observed (Becker et al. 2006, 2011, 2019), which Becker et al. (2019) attributes to the ‘reionization of the CGM’. This behavior is not unexpected given the strong redshift evolution of the UVB towards $z \gtrsim 6$ (Calverley et al. 2011; Wyithe & Bolton 2011; Davies et al. 2018a; D’Aloisio et al. 2018), possibly augmented by the presence of strong UVB fluctuations (Davies & Furlanetto 2016) or a later than expected end to reionization (Kulkarni et al. 2019; Nasir & D’Aloisio 2020; Keating et al. 2020), and offers a preview of the transition from high high-ions to low-ions that one might observe in the IGM writ large. But unfortunately, if one adheres to

¹ This estimate is determined from a CLOUDY photoionization model for an absorber at $z = 6$ at the cosmic mean density with a stopping column density of $\log_{10} N_{\text{HI}} = 15.3$ derived using the scaling relations from (Schaye et al. 2003).

the traditional approach of detecting individual lines, probing IGM absorbers into the reionization epoch is currently beyond current sensitivity limits. As emphasized by Simcoe et al. (2012) and D’Odorico et al. (2013), progress would require either a major observational effort or waiting for the extremely large telescopes.

In this paper we propose a novel statistical approach leveraging methods from precision cosmological studies of the Ly α forest which overcomes this limitation. Whereas early studies of the Ly α forest first treated it as a collection of discrete absorption lines, what precipitated the breakthrough in our understanding of the IGM — that the forest naturally results from hierarchical structure formation in a cold dark matter (CDM) Universe — was the insight that it can instead be analyzed as a continuous cosmological random field. Adopting tools from large-scale structure analysis, cosmologists measured statistics like the transmission probability distribution function (PDF) (e.g. McDonald et al. 2001; Lee et al. 2015), and the power spectrum (e.g. McDonald et al. 2006; Walther et al. 2018, 2019) enabling quantitative analysis and statistical inference that make the Ly α forest a precision probe of cosmological parameters and the nature of dark matter (Seljak et al. 2003; McDonald et al. 2005b; Viel et al. 2013; Palanque-Delabrouille et al. 2015; Iršič et al. 2017).

As opposed to the traditional approach of identifying discrete metal lines in high-redshift quasar spectra, we will treat metal line forests during the EoR analogously, as a continuous field. Actually, measurements along these lines have already been carried out in the context of $z \sim 2$ baryon acoustic oscillation (BAO) measurements using the Ly α forest as a density tracer. Whereas the first such measurements identified the BAO peak at $z \sim 2$ in the 3D Ly α forest correlation function (Busca et al. 2013; Slosar et al. 2013), it was quickly realized (Pieri 2014) that complementary BAO constraints can be obtained by measuring the correlation functions of low-redshift metal-line forests, which has already led to competitive BAO measurements using the C IV forest (Blomqvist et al. 2018) at $z \simeq 2$ and the Mg II forest (du Mas des Bourboux et al. 2019) at $z \simeq 0.6$.

To illustrate the power of this new approach, we focus our attention on the Mg II forest (see also Simcoe et al. 2012) during the EoR². There are several reasons to prefer Mg II over the other low-ions that have been discussed (Oh 2002). First and foremost, Mg II is a doublet absorbing at $\lambda 2796\text{\AA}$ and $\lambda 2804\text{\AA}$ in an approximate 2 : 1 ratio dictated by the ratio of oscillator strengths. This gives rise to a strong correlated absorption feature at a velocity lag $\Delta v_{\text{Mg II}} = 768 \text{ km s}^{-1}$ set by the doublet separation, which provides definitive confirmation that one is actually detecting the Mg II forest and not noise or systematics. Second, the bluer aforementioned ions probe less pathlength because Ly α Gunn-Peterson absorption from the IGM wipes out rest-frame wavelengths blueward of 1216\AA , whereas the redder Mg II transition can probe a much longer line-of-sight

pathlength extending from the quasar redshift down to the redshift at which reionization is complete. Finally, the redder Mg II forest region is expected to be completely uncontaminated by foreground absorption³, whereas for e.g. O I $\lambda 1302$, lower- z absorbers from redder ionic transitions must be identified and masked.⁴

This paper explores the detectability of the Mg II forest during the EoR. Our method for simulating the Mg II forest is described in § 2. The dependence of the Mg II forest correlation function on our model parameters and spectral resolution is studied in § 3, and a method for statistical inference is presented in § 4, along with sensitivity estimates that would result from a hypothetical observing program with the *James Webb Space Telescope* (JWST). CGM absorption associated with galactic metal reservoirs can contaminate the IGM Mg II forest. A model for CGM absorbers is implemented in § 5, we show how this CGM absorption alters the flux PDF of the Mg II forest in § 6, and implement a procedure for identifying and masking CGM absorbers in § 7. We summarize and conclude in § 8.

Throughout this work we adopt a Λ CDM cosmology with the following parameters: $\Omega_{\text{m}} = 0.3192$, $\Omega_{\Lambda} = 0.6808$, $\Omega_{\text{b}} = 0.04964$, $h = 0.67038$, which agree with latest cosmological constraints from the CMB (Planck et al. 2018) within one sigma. All distances are quoted in comoving units denoted as cMpc or ckpc. In this cosmology, a line-of-sight velocity of $v_{\parallel} = 100 \text{ km s}^{-1}$ corresponds to $r_{\parallel} = \frac{v_{\parallel}}{aH(z)} = 0.90 \text{ cMpc}$ in the Hubble flow at $z = 7.5$. All equivalent widths are in the rest-frame in units of \AA and are denoted by the symbol W_{λ} . For doublet transitions the equivalent width of the stronger transition in the doublet are quoted.

2 SIMULATING THE MG II FOREST

2.1 General Considerations

To simulate the Mg II forest we need to model the distribution of metals in the IGM during the reionization phase transition. This is clearly an extreme challenge to simulate, as one must capture not only the physical state of the reionizing IGM, but also the production and dispersal of metals, and their ionization state. While progress on simulating all of this complex physics has been made in recent years (e.g. Oppenheimer et al. 2009; Pallottini et al. 2014; Pawlik et al. 2017; Jaacks et al. 2018, 2019; Doughty & Finlator 2019; Kirihara et al. 2020), our goal here is to investigate detectability and perform a sensitivity analysis. To this end we adopt a

² Although Mg II is singly ionized, because the Mg I ionization edge (0.56 Rydberg) lies below 1 Rydberg, low IGM densities and the star-formation powered UVB imply Mg will entirely populate the Mg II state in a neutral IGM. See the next section for additional details.

³ The only strong resonant lines that could potentially contaminate the Mg II forest are the Ca II H+K doublet $\lambda 3969$, $\lambda 3934$ and Na I $\lambda 5897$. But these absorbers are extremely weak (Zhu & Ménard 2013), because they are not the dominant ionization state of either element in the presence of a radiation field that cuts off at energies exceeding the Lyman limit, as is the case in the neutral IGM. These lines are thus only observable in rare extremely strong absorbers where dust can attenuate the ionizing continuum redward of the Lyman limit.

⁴ For example for a quasar at $z_{\text{QSO}} = 7.5$ there would be contamination from Mg II at $z \sim 2.9$, Al II $\lambda 1670$ at $z \sim 5.5$, C IV $\lambda 1548$ and Si II $\lambda 1526$ at $z = 6.1$, etc.

highly simplistic toy model whereby the entire IGM is suffused with metals at a fixed metallicity Z with solar relative abundances.

While in principle ionization corrections would be required to determine the fraction of Mg in the Mg II state, this can be trivially simplified. Note that ionization edge of Mg I is at 0.56 Rydberg which lies below the 1 Rydberg ionizing edge for hydrogen, whereas the Mg II edge is at 1.11 Rydberg blueward of the Lyman edge. The IGM is thus essentially completely transparent at the energies that ionize neutral Mg, and it is expected that even prior to reionization, the ultraviolet radiation field sourced by cosmic star-formation will produce a metagalactic UV background sufficiently intense at the Mg I edge to ionize all Mg into the Mg II state. We explicitly checked this by running a CLOUDY (Ferland et al. 2017) model with gas at the mean density of the IGM at $z = 7.5$ subjected to a Haardt & Madau (2012) UV background truncated at energies greater than 1 Rydberg. We find negligible $\lesssim 10^{-8}$ abundance of Mg in any ionization state besides Mg II irrespective of the total N_{H} used to set the so-called stopping criterion. Thus for the purposes of the present study it is an excellent approximation to assume that the ionization state of Mg is simply tied to that of hydrogen, and neutral regions of the Universe are in the Mg II state.

Having described our model of the metallicity and ionization state of Mg, we now turn to modeling the IGM during reionization. It is well known that reionization photoheating modifies the small-scale structure of the IGM. Although baryons trace dark matter fluctuations on large scales, on smaller scales gas is supported against gravitational collapse by thermal pressure. Analogous to the classic Jeans argument, baryonic fluctuations are suppressed relative to the pressureless dark matter, and gas is ‘pressure smoothed’ or ‘filtered’ on small scales (Gnedin & Hui 1998; Kulkarni et al. 2015; Rorai et al. 2017). As a result, the small-scale structure or clumpiness of the pre-reionization IGM is intimately related to its thermal evolution. It is currently unknown whether the IGM adiabatically cooled to extremely low temperatures $T \lesssim 1$ K just before reionization at $z \sim 7-8$, or if a metagalactic X-ray background, sourced by faint AGN (Madau et al. 2004; Ricotti & Ostriker 2004), X-ray binaries (Madau & Fragos 2017), or Pop III stellar remnants (Xu et al. 2016), photoelectrically heated it to much higher temperatures $T \sim 1000$ K (e.g. Furlanetto 2006b, but see Fialkov et al. (2014)). During reionization ionization fronts propagate supersonically through the IGM, impulsively heating reionized gas to $\sim 10^4$ K. This rapid temperature increase drives the Jeans scale from ~ 1 ckpc (for $T \lesssim 1$ K) up to ~ 100 ckpc, dissipating pre-reionization IGM small-scale structure on a timescale of ~ 1 Gyr (D’Aloisio et al. 2020; Davies & Hennawi 2020).

Since the Mg II forest absorption arises from neutral regions of the IGM, in principle predicting its clustering strength depends on the small-scale structure of the IGM, and hence on the pre-reionization IGM temperature evolution. Accurately simulating the pre-reionization IGM is a daunting numerical problem (D’Aloisio et al. 2020; Davies & Hennawi 2020). Ideally, the simulation domain would be sufficiently large ($\gtrsim 10$ cMpc) to remain linear in its fundamental mode, and encompass the 768 km s^{-1} (6.9 cMpc) doublet separation of Mg II and typical size (~ 10 cMpc) of ion-

ized bubbles, while simultaneously resolving the extremely small ~ 1 ckpc Jeans scale corresponding to the potentially very low temperatures $T \lesssim 1$ K prevailing in the pre-reionization IGM. Naively, this would require a $\sim 20,000^3$ grid or comparable number of SPH particles, unattainable even with the world’s largest supercomputers. Given our lack of knowledge of pre-reionization IGM temperature evolution, and the numerical challenge, we will utilize a snapshot of a hydrodynamical simulation at $z = 7.5$ prior to reionization photoheating. This simulation, of a $L_{\text{box}} = 40 h^{-1}$ cMpc ($v_{\text{box}} \equiv aH(z)L_{\text{box}} = 6600 \text{ km s}^{-1}$ at $z = 7.5$) domain on a 2048^3 grid, has a grid scale of 29 ckpc (3.2 km s^{-1}), which would fail to resolve the ~ 1 ckpc Jeans scale for pre-reionization IGM temperatures $T \lesssim 1$ K, but marginally resolve the ~ 30 ckpc Jeans scale if an X-ray background preheated the IGM to $T \sim 1000$ K.

As this paper focuses on the clustering of the Mg II forest which is tied to the clustering of the IGM via our simple enrichment model, a discussion of the impact of this unresolved structure on our results is in order. Unlike the Gunn-Peterson optical depth for H I Ly α absorption, which probes neutral gas in an ionized medium and hence scales $\tau_{\text{Ly}\alpha} \propto n_{\text{H I}} \propto n_{\text{H}}^2$ quadratically with density, the analogous optical depth for the Mg II forest $\tau_{\text{Mg II}} \propto n_{\text{Mg II}} \propto n_{\text{H I}} \propto n_{\text{H}}$ scales only linearly with density, because the medium is predominantly neutral. Thus if $F = e^{-\tau_{\text{Mg II}}}$, $\delta_f \equiv (F - \langle F \rangle) / \langle F \rangle \approx \tau_{\text{Mg II}} \propto n_{\text{H}}$ is always a good approximation for the small optical depths we consider, the Mg II forest flux correlation function, $\xi_{\text{Mg II}} \equiv \langle \delta_f \delta_f \rangle \propto \xi_{\rho, 1\text{D}}$, is simply proportional to the correlation function of the overdensity projected along skewers, which can in turn be written as the Fourier transform

$$\xi_{\rho, 1\text{D}}(r) = \int_0^\infty \Delta_{\rho, 1\text{D}}^2(k) \cos(kr) d \ln k. \quad (1)$$

of the analogous 1D density dimensionless power spectrum $\Delta_{\rho, 1\text{D}}^2(k) \equiv k P_{\rho, 1\text{D}}(k) / \pi$. The dimensionless power $\Delta_{\rho, 1\text{D}}^2(k)$ is a smoothly rising function that traces the underlying clustering of the CDM, but is truncated by a sharp cutoff at the Jeans scale of the pre-reionization IGM. Failure to resolve this Jeans scale would then effectively truncate $\Delta_{\rho, 1\text{D}}^2(k)$ at the simulation grid scale $k_{\text{trunc}} \approx 2\pi / r_{\text{grid}}$. Note that the $\cos(kr)$ factor in eqn. (1) implies that only wavenumbers with $kr \lesssim 1$ for which $\cos(kr) \sim 1$ contribute significantly to the integral, whereas wavenumbers $kr \gg 1$ contribute negligibly because of cancellations induced by the highly oscillatory $\cos(kr)$ term. In other words, only Fourier modes with wavelengths $\lambda \gtrsim r$ ($k \lesssim 2\pi / \lambda$) larger than the scale of interest contribute to the correlation function. Since the velocity separations (length scales) that we would realistically probe with real data ($\gtrsim 30 \text{ km s}^{-1}$) correspond to spatial scales at least an order of magnitude larger than the pre-reionization IGM Jeans scale ($\sim 1-30$ ckpc or $\sim 0.1-3 \text{ km s}^{-1}$), we do not expect this missing small-scale power to have a significant impact on our results.

2.2 Hydrodynamical Simulations of the Pre-Reionization IGM

We simulate the Mg II forest using *Nyx*, a massively parallel N-body gravity + grid hydrodynamics code specifically designed for simulating the IGM (Almgren et al. 2013; Lukić

et al. 2015). Initial conditions were generated using the MUSIC code (Hahn & Abel 2011) using a transfer function generated by CAMB (Lewis et al. 2000; Howlett et al. 2012). We assumed a Λ CDM cosmology with the following parameters: $\Omega_m = 0.3192$, $\Omega_\Lambda = 0.6808$, $\Omega_b = 0.04964$, $h = 0.6704$, $\sigma_8 = 0.826$ and $n_s = 0.9655$ which agree with latest cosmological constraints from the CMB (Planck et al. 2018) within one sigma. We adopted hydrogen and helium mass abundances ($X_p = 0.76$ and $Y_p = 0.24$) in agreement with the recent CMB observations and Big Bang nucleosynthesis (Coc et al. 2014). We simulated a domain with a box size of $40 \text{ cMpc } h^{-1}$ using a 2048^3 grid, and the simulation was started at $z_{\text{ini}} = 159$.

We analyze a snapshot at $z = 7.5$, which is prior to the redshift of reionization in this simulation. Specifically, hydrodynamical simulations like Nyx which do not attempt to model reionization (but see Oñorbe et al. 2017, 2019) typically treat reionization by assuming a spatially uniform, time-varying metagalactic UVB radiation field, input to the code as a list of photoionization and photoheating rates that vary with redshift. The simulation we analyze reionizes at $z = 6.0$, which is to say that the UVB is turned on at this redshift, which occurs at a later time than the snapshot we analyze at $z = 7.5$. For additional details about the numerical approach see Oñorbe et al. (2019). The simulation analyzed here is similar to the ‘flash’ reionization simulations in that paper, where flash refers to the fact that the UVB is abruptly turned on at $z = 6.0$ causing the simulation to instantaneously reionize.

2.3 Semi-Numerical Reionization Topology

Our Nyx hydrodynamical simulation yields the baryon density, peculiar velocity, and temperature at each grid cell. The only other quantity required to simulate the Mg II forest is the hydrogen neutral fraction x_{HI} . For this we must create a model of the global reionization topology in the simulation domain. To generate the H I neutral fraction x_{HI} throughout the simulation we use a modified version of the semi-numerical reionization code 21cmFAST⁵ (Mesinger et al. 2011), to be presented in further detail in Davies & Furlanetto (in prep.). The semi-numerical approach computes the fraction of material that has collapsed into dark matter halos, f_{coll} , following conditional Press-Schechter (Lacey & Cole 1993) applied to an approximate non-linear density field computed by applying the Zel’dovich approximation (Zel’dovich 1970) to the initial conditions of the Nyx simulation, and evolving it to $z = 7.5$. A region is considered ionized if $f_{\text{coll}} > \zeta^{-1}$ on *any* scale, where ζ is the ‘ionizing efficiency,’ which combines several parameters governing the efficiency of star formation and the production and escape of ionizing photons from galaxies into a single parameter that corresponds to the total number of ionizing photons emitted per collapsed baryon. An ionizing mean free path λ_{mfp} is implemented by suppressing the contribution of ionizing photons with a smooth exponential decline rather than the traditional hard cutoff (R_{max}). The neutral fraction x_{HI} is computed on a 256^3 grid encompassing the Nyx simulation domain, which is chosen to be sufficiently fine to sample the ionization topology but also coarse enough to guarantee

sufficient numbers of dark matter halos (which source the ionizing photons) in each cell.

We generated a sequence of 51 different reionization topologies, parameterized by the volume filling fraction of neutral hydrogen $\langle x_{\text{HI}} \rangle$ at $z = 7.5$, spanning the range $\langle x_{\text{HI}} \rangle = 0.0$ to 1.0 in steps of 0.02 . The models used here adopted an ionizing photon mean free path $\lambda_{\text{mfp}} = 20 \text{ cMpc}$, and the ionizing efficiency was then adjusted to get the full range of $\langle x_{\text{HI}} \rangle$ required. For additional details about the semi-numerical reionization model see Davies et al. (2018b), Oñorbe et al. (2019), and Davies & Furlanetto, in prep.

2.4 Creating Mg II Forest Skewers

To simulate the Mg II forest we generate skewers by drawing random locations along one face of the simulation cube, and record the baryon density, the line-of-sight component of the peculiar velocity field, the temperature, and neutral fraction at each line-of-sight location in the grid, where the latter comes from the semi-numerical reionization topology just described. The doublet nature of the Mg II ion requires that we deal with resonant absorption at two wavelengths $\lambda_{2796}, \lambda_{2804\text{\AA}}$, which corresponds to a velocity difference of $\Delta v = 768 \text{ km s}^{-1}$. In practice we compute the optical depth τ_{2796} for the stronger λ_{2796} transition, and then rescale this array by the oscillator strength ratio of $f_{2804}/f_{2796} = 0.497$ to obtain τ_{2804} , which we shift by the doublet separation Δv , allowing us to compute the total optical depth $\tau_{\text{Mg II}} = \tau_{2796} + \tau_{2804}$. Below we describe our approach for generating skewers of τ_{2796} , the optical depth in the $\lambda_{2796\text{\AA}}$ resonance.

The optical depth for resonant absorption for an ionic transition X^{n+} of an element X in its n th ionization state is

$$\tau_\nu = \int n_X x^{n+} \sigma_\nu dr, \quad (2)$$

where ν is the frequency, n_X is the number density of the element X , x^{n+} is the fraction of this element populating the n th ionization state, and

$$\sigma_\nu = \frac{\pi e^2}{m_e c} f_{\ell u} \phi_\nu \quad (3)$$

is the frequency specific cross-section. Here e and m_e are the electron charge and mass, respectively, c is the speed of light, $f_{\ell u}$ is the oscillator strength for the resonant transition $\ell \rightarrow u$ at rest-frame frequency $\nu_{\ell u}$, and ϕ_ν is the line profile. Whereas in general ϕ_ν is described by the Voigt profile, for the extremely low optical depths characterizing metal-line forests it is a very good approximation to represent ϕ_ν with a Gaussian form

$$\phi_\nu = \frac{1}{\sqrt{\pi}} \Delta\nu_D \exp \left[- \left(\frac{\nu - \nu_{\ell u}}{\Delta\nu_D} \right)^2 \right], \quad (4)$$

where $\Delta\nu_D = (b/c)\nu_{\ell u}$ is the Doppler frequency width of the Gaussian profile determined by the Doppler parameter $b = \sqrt{2k_B T/m_X}$ characterizing thermal broadening of the absorption lines, where k_B is Boltzmann’s constant and m_X is the mass of element X .

If we assume, as we will throughout this work, that the metal line species X is uniformly mixed with the baryons in the IGM, then we can write $n_X = \langle n_X \rangle \Delta$, where $\Delta \equiv \rho_B / \langle \rho_B \rangle$, ρ_B is baryon mass density, angle brackets represent

⁵ <https://github.com/andreimesinger/21cmFAST>

an average over the volume of the Universe, and $\langle n_X \rangle = Z/Z_\odot (n_X/n_H)_\odot \langle n_H \rangle$, where Z/Z_\odot is the metallicity in solar units, and $(n_X/n_H)_\odot$ is the abundance of element X in the sun.

Combining eqns. 2-4, and transforming to velocity coordinates using the Doppler formula $\nu' = \nu_{\ell u}[1 - (v' - v)/c]$ and the Hubble relation $dr = dv/H(z)$, where $H(z)$ is the Hubble expansion rate at redshift z , we finally arrive at

$$\tau_v = \tau_{X,0} \int \frac{x^{n+\Delta}}{\sqrt{\pi}} \exp\left[-\left(\frac{v' - v}{b}\right)^2\right] \frac{dv'}{b}, \quad (5)$$

where we have defined $\tau_{X,0}$ the metal-line forest analog of the Gunn-Peterson optical depth (Oh 2002),

$$\tau_{X,0} = \frac{\pi e^2 f_{\ell u} \lambda_{\ell u} \langle n_X \rangle}{m_e c H(z)} \quad (6)$$

or plugging in numbers for the Mg II forest

$$\tau_{X,0} = 0.06 \left(\frac{Z/Z_\odot}{10^{-3}}\right) \left(\frac{(n_X/n_H)_\odot}{3.4 \times 10^{-5}}\right) \left(\frac{f_{\ell u}}{0.62}\right) \left(\frac{\lambda_{\ell u}}{2796 \text{ \AA}}\right) \left(\frac{1+z}{8.5}\right)^{3/2}, \quad (7)$$

where we used the Mg abundance $(n_{\text{Mg}}/n_H)_\odot = 3.4 \times 10^{-5}$ determined from the solar photosphere (Asplund et al. 2009), and the oscillator strength f_{2796} and wavelength $\lambda_{\ell u}$ of the stronger Mg II $\lambda 2796 \text{ \AA}$ transition.

Special attention must be paid to the construction of metal-line forest skewers because of the extremely small Doppler parameters b . This results from both cold pre-reionization IGM temperatures and the fact that metals are much heavier than hydrogen. The temperature of the pre-reionization IGM is currently unknown and could be anywhere in the range $T \sim 1 - 1000 \text{ K}$, as discussed in § 2.1. Plugging in numbers for the Doppler parameter for an ion X

$$b = 0.26 \text{ km s}^{-1} \left(\frac{T}{100 \text{ K}}\right)^{-1/2} \left(\frac{m_X/m_H}{24}\right)^{-1/2}, \quad (8)$$

where we normalized using the atomic weight of Mg. The Nyx hydrodynamical simulations employed in this work have a grid scale of $dv = 3.2 \text{ km s}^{-1}$ at $z = 7.5$, thus the thermal broadening of Mg II forest absorption lines are far from being resolved by our native velocity grid. One option would be to interpolate the simulated density and temperature fields onto a much finer grid before performing the convolution in eqn. (5) required to construct simulated Mg II forest skewers, but this is computationally intensive given the small b parameters one would need to resolve. Instead, we adopt the clever approach described in Appendix B of Lukić et al. (2015), which is far faster because it enables one to work on the native grid, but nevertheless explicitly conserves optical depth. Specifically, we discretize the integral in eqn. (5), taking the overdensity and temperature as constant across each grid cell. For the k th pixel at velocity $v_k = kv$ in the Hubble expansion, the optical depth is

$$\tau_{v_j} = \tau_{X,0} \sum_i \frac{x_i^{n+\Delta_i}}{2} [\text{erf}(y_{i-1/2}) - \text{erf}(y_{i+1/2})], \quad (9)$$

where the error function⁶ results from the integral of the

Gaussian profile across the i th pixel (from $v_{i-1/2}$ to $v_{i+1/2}$), and $y_{i-1/2} = (v_j - v_{\parallel,i} - v_{i-1/2})/b$, where $v_{\parallel,i}$ is the component of the gas peculiar velocity parallel to the sightline, $v_{i-1/2} = (i - 1/2)dv$, and an analogous expression holds for $y_{i+1/2}$.

2.5 Generating the Model Parameter Grid

Our goal is to construct a large set of Mg II forest skewers for a model grid governed by two parameters, [Mg/H] and $\langle x_{\text{H I}} \rangle$. We start with 10,000 skewers of Δ , v_{\parallel} , and T , extracted from the Nyx simulation at random locations along one face of the cube. For the $x_{\text{H I}}$ field, we use the set of 51 reionization topologies in the range $\langle x_{\text{H I}} \rangle = 0.0$ to 1.0. Given that the Mg II forest optical depth $\tau_{\text{Mg II}}$ is linear in Z (see eqn. 6), which we define as $Z/Z_\odot \equiv 10^{[\text{Mg}/\text{H}]}$, we perform the convolutions in eqn. (9) for each value of $\langle x_{\text{H I}} \rangle$, but a single metallicity, and scale the resulting optical depth to the desired metallicity. For the metallicity grid we use 201 models spanning the range [Mg/H] = [-6.0, -2.0]. The result of this procedure is a set of 10,000 Mg II forest skewers generated for a grid of $51 \times 201 = 10,251$ models.

2.6 Forward Modeling Observed Data

For the purpose of visualizing real observational data and performing statistical inference we create mock spectra with smearing induced by finite spectral resolution and add noise consistent with a realistic S/N ratio. We parameterize the data quality with the FWHM of the spectral resolution assuming a Gaussian line spread function, and the S/N per pixel, where the spectral sampling is assumed to be $n_{\text{samp}} = 3$ pixels per spectral resolution element of width the FWHM. Our simulated spectra are convolved with a Gaussian consistent with the spectral resolution, interpolated onto a velocity grid set by the spectral sampling, and then Gaussian random noise is added with a standard deviation $\sigma_{\text{S/N}} = (\text{S/N})^{-1}$.

For a quasar at $z = 7.5$, and considering a redshift interval of $\Delta z = 0.6$ from $z = 6.9 - 7.5$ where we expect the Universe to be significantly neutral, the Mg II forest is redshifted to observed frame wavelengths of $\lambda = 2.21 - 2.38 \mu\text{m}$ in the K -band. In this work we model spectra from JWST/NIRSpec for which the sky background at the relevant wavelengths comes from zodiacal light and is relatively smooth. For this case, assuming spectral noise that is constant with wavelength is a reasonable approximation. On the other hand, ground-based observations of this spectral region would have heteroscedastic noise owing to the forest of atmospheric OH airglow lines. As we will aim to measure the two-point correlation function of the Mg II forest (see § 3), formally the noise in the estimated correlation function averages to zero at all non-zero velocity lags irrespective of whether or not it is heteroscedastic. As such, even for ground-based observations, we do not expect the heteroscedasticity of the noise to be a significant issue⁷, provided that one take our assumed S/N ratio to be a suitable average over the spectral region in question.

We primarily focus on mock data with FWHM = 100 km s^{-1} and S/N = 100, representative of what can be

⁶ Note that equivalent eqn. B5 in Lukić et al. (2015) is missing a factor of 1/2

⁷ This assumes that correlated noise resulting from sky subtraction systematics are insignificant, which we expect to be the case.

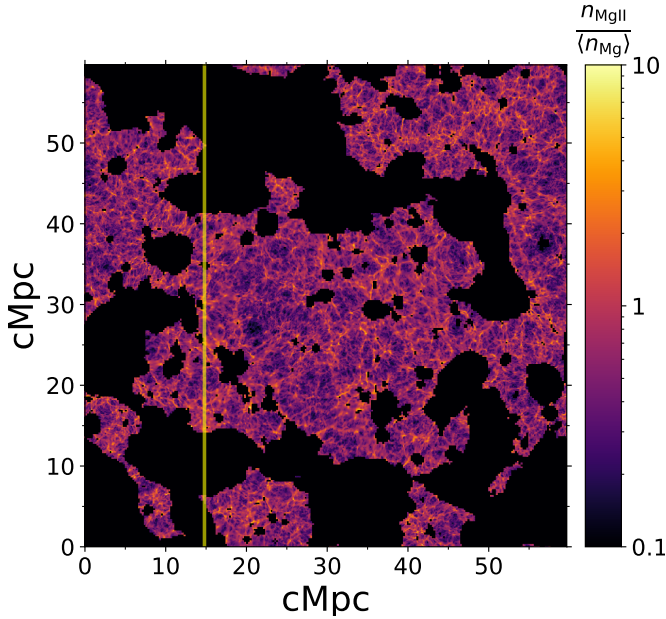


Figure 1. The topology of Mg II absorbing gas. The image is a single pixel wide (29 ckpc) slice through our simulation of the distribution of Mg II for a universe with a volume averaged neutral fraction $\langle x_{\text{H I}} \rangle = 0.50$ at $z = 7.5$. The quantity plotted is $x_{\text{H I}} \Delta$ where $\Delta = \rho / \langle \rho_B \rangle$ which is equivalent to $n_{\text{Mg II}} / \langle n_{\text{Mg}} \rangle$ given our assumption of a uniform metallicity distribution and $x_{\text{H I}} = x_{\text{Mg II}}$ (see § 2.1). The color scale is logarithmic, as indicated by the colorbar at right. Black regions have been reionized, whereas colored regions are still neutral. The vertical yellow line shows a skewer through the volume for which Mg II forest absorption spectra are shown in Fig. 2

achieved with JWST/NIRSpec in a 10hr integration for a typical $z \gtrsim 7$ quasar with an AB apparent magnitude of $m_{1450} = 20.5$, chosen to correspond to the observed frame J -band. This estimate is based on calculations performed with the JWST/NIRSpec exposure time calculator⁸.

2.7 Results

The topology of Mg II absorbing gas predicted by our model is shown in Fig. 1 for a universe with a volume averaged neutral fraction $\langle x_{\text{H I}} \rangle = 0.50$ at $z = 7.5$. The figure shows a single pixel (29 ckpc) slice through $x_{\text{H I}} \Delta$, which is equivalent to $n_{\text{Mg II}} / \langle n_{\text{Mg}} \rangle$ given our assumption of a uniform metallicity distribution and $x_{\text{H I}} = x_{\text{Mg II}}$ (see § 2.1). The vertical yellow line shows a skewer through this volume taken to be the line-of-sight direction towards the observer. Fig. 2 shows our predictions for the Mg II forest spectra along this sightline. The top panel shows the baryon overdensity, which traces the clumpy structure of the pre-reionization IGM determined by the underlying CDM as discussed in § 2.1. The second panel from the top shows the IGM neutral fraction, $x_{\text{H I}}$, from our semi-numerical reionization topology. The lower panels show the simulated Mg II forest for various values of [Mg/H], where the red curves are perfect spectra and black histograms show realistic mock JWST/NIRSpec spectra with

a resolution $\text{FWHM} = 100 \text{ km s}^{-1}$ and $\text{S/N} = 100$ per pixel (see § 2.6 for details).

3 THE CORRELATION FUNCTION OF THE MG II FOREST

It is clear from the mock observations in Fig. 2 that even with the exquisite spectra delivered by JWST, the traditional approach of detecting individual Mg II absorption systems appears hopeless. Nevertheless, the Mg II forest is still detectable by statistically averaging down the noise to reveal the correlated structure present. To this end, we compute the two-point correlation function of the transmission, which has two important advantages. First, since the spectrograph and background noise are white, the noise covariance averages down to be consistent with zero at all non-zero lags $\Delta v > 0$. Second, the weak absorption field is highly correlated at the doublet separation $\Delta v_{\text{Mg II}} = 768 \text{ km s}^{-1}$, which will give rise to a pronounced peak in the correlation function at this velocity lag.

Specifically, if F is the continuum normalized flux, we define the relative flux fluctuation

$$\delta_f \equiv \frac{F - \langle F \rangle}{\langle F \rangle}, \quad (10)$$

where $\langle F \rangle$ is the mean flux. We then compute the correlation function

$$\xi(\Delta v) = \langle \delta_f(v) \delta_f(v + \Delta v) \rangle \quad (11)$$

by averaging over all pairs of pixels separated by velocity lag Δv .

3.1 Dependence on Model Parameters

The correlation function $\xi(\Delta v)$ is shown in Fig. 3 for several different combinations of metallicity, [Mg/H], and volume averaged neutral fraction, $\langle x_{\text{H I}} \rangle$. For this computation we have assumed noiseless data, and a resolution of $\text{FWHM} = 30 \text{ km s}^{-1}$ typical of a ground based echelle spectrograph.

There are several important features of the correlation function shown in Fig. 3 which we now describe. First, because pre-reionization IGM baryons trace the clumpy small-scale structure set by the underlying CDM, there is significant variance on small scales and as a result the Mg II forest correlation function exhibits a precipitous rise towards small velocity lags. Second, there is a strong peak at the doublet separation $\Delta v_{\text{Mg II}} = 768 \text{ km s}^{-1}$, indicated by the red vertical dashed line, which arises from the doublet nature of the Mg II transition. The height of this peak is a result of the significant small-scale power, since pixels separated by around $\Delta v_{\text{Mg II}} = 768 \text{ km s}^{-1}$ are in reality probing correlated fluctuations in the gas at much smaller velocity lags. Finally, at intermediate to large velocity lags $\xi(\Delta v)$ exhibits an overall power-law dependence on $\Delta v_{\text{Mg II}}$, which appears to be highly sensitive to the value of $\langle x_{\text{H I}} \rangle$. This occurs because line-of-sight fluctuations in neutral fraction $x_{\text{H I}}$ (see Fig. 2 second panel from top) modulate the Mg II forest sourcing fluctuations on a hierarchy of scales set by the topology of the neutral regions during reionization (see Fig. 1).

Naively one might expect a perfect degeneracy between the global neutral fraction $\langle x_{\text{H I}} \rangle$ and Mg abundance [Mg/H],

⁸ <https://jwst.etc.stsci.edu/>

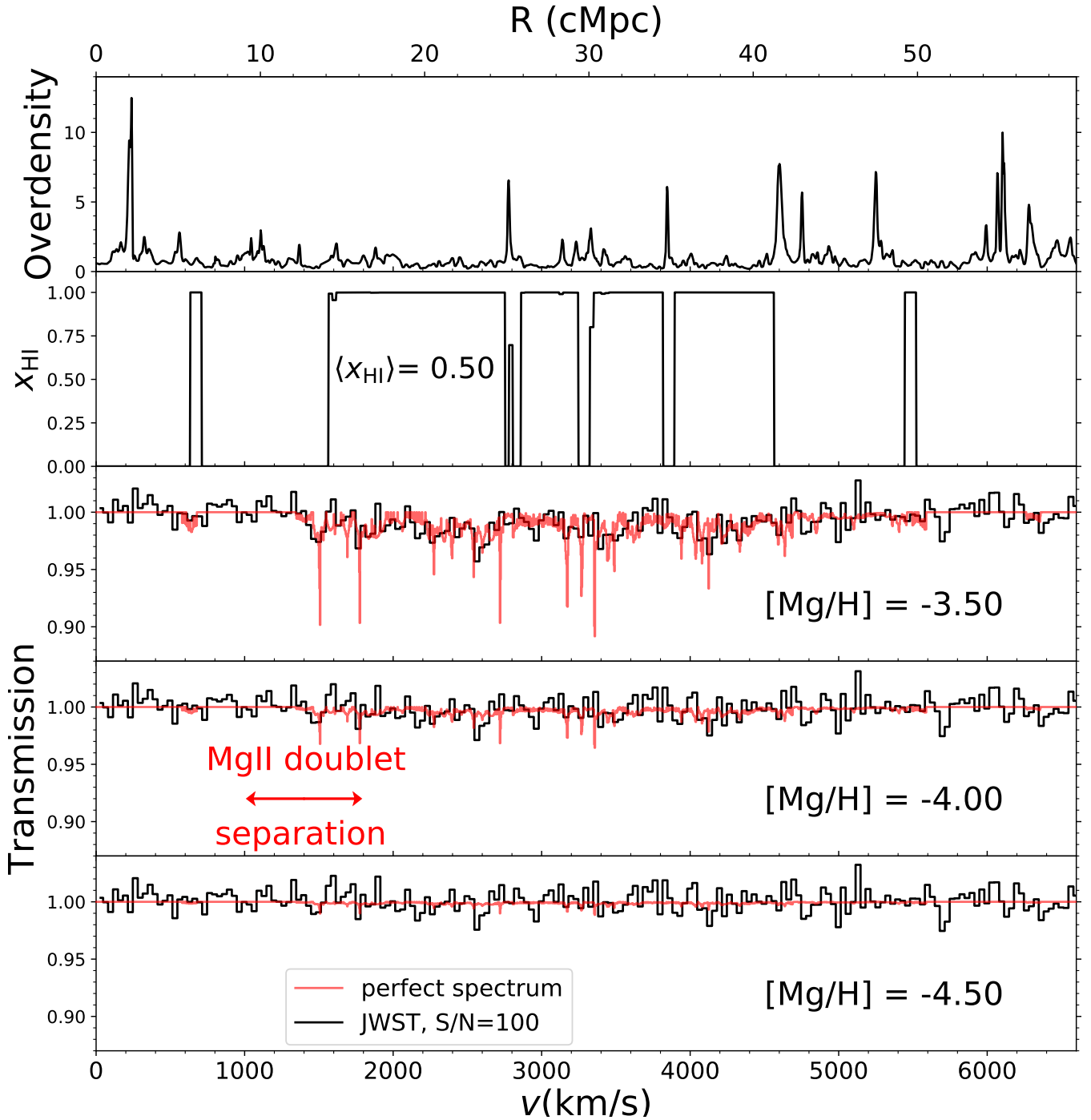


Figure 2. Simulations of the MgII forest for a skewer indicated by the yellow vertical line in Fig. 1. *Top:* Baryon overdensity along the skewer obtained from a hydrodynamical simulation of the $z = 7.5$ pre-reionization IGM. *Second from Top:* The IGM neutral fraction x_{HI} along the skewer determined from a semi-numerical reionization model with $\langle x_{\text{HI}} \rangle = 0.5$. *Lower Panels:* Simulated MgII forests for various values of $[\text{Mg}/\text{H}]$ (relative to solar), for perfect spectra (red curves) and realistic mock JWST/NIRSpec spectra (black histograms; FWHM=100 km s⁻¹, S/N = 100 per pixel) for ~ 10 hr of exposure per source for quasars comparably bright as the two known at $z = 7.5$.

since the optical depth for the MgII forest in eqn. (5) depends on the degenerate product of x_{HI} and $[\text{Mg}/\text{H}]$. However, this naive intuition proves incorrect, as is clear by comparing the solid, $\langle x_{\text{HI}} \rangle = 0.9$, and dotted, $\langle x_{\text{HI}} \rangle = 0.2$, curves in Fig. 3. At fixed $\langle x_{\text{HI}} \rangle$, the amplitude of the correlation function scales as the square of the Mg abundance $[\text{Mg}/\text{H}]$, as expected from eqn. (5) and eqn. (11) — when F is small

$|\delta_f| \approx |\tau - \langle \tau \rangle|$, and thus $\xi \propto \delta_f^2 \propto \tau_{\text{MgII}}^2$. But the dependence of $\xi(\Delta v)$ on x_{HI} is more complex, which probes large-scale $\sim 1 - 30$ cMpc fluctuations arising from the global topology of reionization.

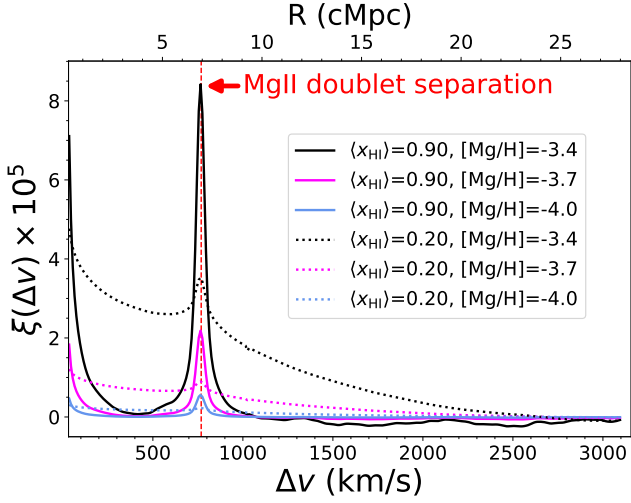


Figure 3. Predicted MgII forest correlation function. Curves show the correlation function $\xi(\Delta v)$ of the relative flux fluctuation δ_f (see eqn. 10) where colors show different IGM enrichment [Mg/H], whereas solid and dotted curves show average IGM neutral fractions of $\langle x_{\text{HI}} \rangle = 0.9$ and $\langle x_{\text{HI}} \rangle = 0.2$, respectively. The correlation function exhibits a conspicuous peak at $\Delta v = 768 \text{ km s}^{-1}$ corresponding to the MgII doublet separation, indicated by the vertical red dashed line. Because the correlation function shape has a distinct dependence on each of these parameters they can both be independently measured. A spectral resolution of $\text{FWHM} = 30 \text{ km s}^{-1}$ typical of a ground based echelle spectrograph has been assumed.

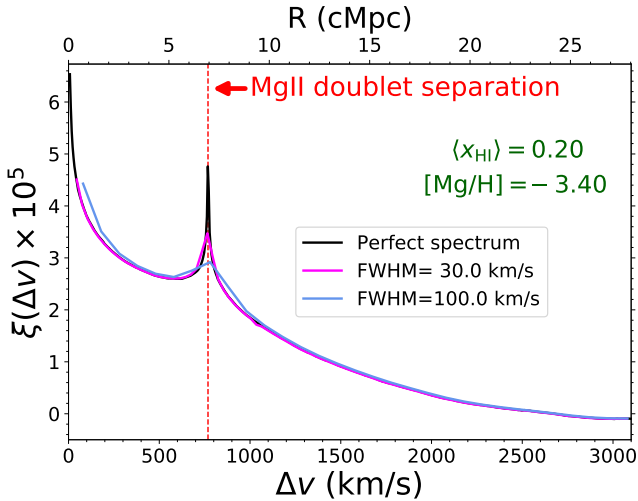


Figure 4. Impact of spectral resolution on the MgII forest correlation function. Curves show the correlation function $\xi(\Delta v)$ of the transmission observed at different spectral resolutions. Whereas the black curve represents perfect resolution (i.e. the highest resolution we can model with our current simulations), the magenta (FWHM = 100 km s^{-1} ; e.g. JWST) and blue (FWHM = 30 km s^{-1} ; ground-based) curves illustrate what can be achieved at moderate and echelle spectral resolution, respectively. The impact of finite spectral resolution is to smooth out the rise in the small-scale power at velocity lags smaller and comparable to the FWHM, and to broaden the peak in the correlation function at the doublet separation.

3.2 Dependence on Resolution

In Fig. 4 we illustrate the impact of spectral resolution on $\xi(\Delta v)$ for a model with $[\text{Mg}/\text{H}] = -3.4$ and $\langle x_{\text{HI}} \rangle = 0.2$. Finite spectral resolution smears out the small-scale structure in the MgII forest reducing the amount of variance at velocity lags smaller than the FWHM of the spectrograph. This is readily apparent from the curves in Fig. 4, where one sees that the rise in the correlation function has been smoothed out at velocity lags comparable to the spectral resolution. Because the peak in the correlation function at the doublet separation $\Delta v = 768 \text{ km s}^{-1}$ also results from small-scale correlations (see discussion in § 3.1), we observe that this peak is broadened by the spectral smearing and its resulting width is effectively determined by the spectral resolution. The black curves (labeled Perfect Spectrum) have not been explicitly smoothed to model spectral resolution, however the small-scale power is nevertheless smoothed by the finite spatial resolution of our simulation, which has a grid scale of 29 ckpc corresponding to 3.2 km s^{-1} in the Hubble flow. As discussed in § 2.1, our simulations will not resolve the small-scale structure of the IGM if pre-reionization baryons are at temperature $T \lesssim 1000 \text{ K}$ resulting in a Jeans scale smaller than our grid scale. However, we expect this smoothing to only impact the correlation function at velocity lags smaller than the grid scale 3.2 km s^{-1} (see eqn. 1). But measuring lags this small would require high-resolution near-IR spectra which we do not consider here.

4 STATISTICAL INFERENCE

To assess the precision with which model parameters can be measured from real observational data we construct mock observations and perform statistical inference.

4.1 The Mock Dataset

We consider a realistic mock dataset of $n_{\text{QSO}} = 10$ quasar spectra, each covering a pathlength of $\Delta z = 0.6$ of the MgII forest, resulting in a total pathlength of $\Delta z_{\text{tot}} = n_{\text{QSO}} \times \Delta z = 6.0$. Our forward modeled spectra have a velocity extent of 6567 km s^{-1} set by how our simulation box fits onto the spectral velocity grid, which is far smaller than the $21,936 \text{ km s}^{-1}$ corresponding to $^9 \Delta z = 0.6$. We thus create a mock dataset with the same effective pathlength by aggregating the equivalent integer number of shorter 6567 km s^{-1} skewers. In other words, we model our mock dataset comprising of $n_{\text{QSO}} = 10$ quasars with $\Delta z = 0.6$ and desired pathlength of $\Delta z_{\text{tot}} = 6.0$, with an integer number of $n_{\text{path}} = 33$ skewers, corresponding to a slightly shorter pathlength of $\Delta z_{\text{tot}} = 5.93$. As described in § 2.6, we parameterize the data quality with the spectral resolution FWHM and the S/N ratio, and here consider observations with JWST/NIRSpec and assume $\text{FWHM} = 100 \text{ km s}^{-1}$ and $\text{S/N} = 100$.

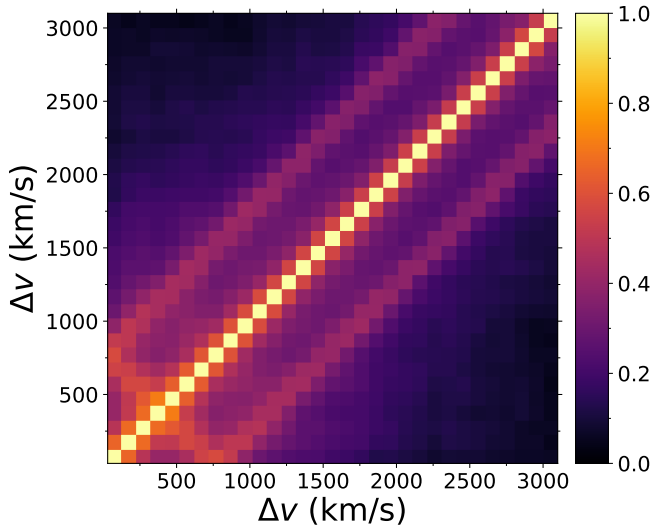


Figure 5. Correlation matrix of the Mg II forest correlation function. Correlation matrix for a model with $\langle x_{\text{H I}} \rangle = 0.74$ and $[\text{Mg}/\text{H}] = -3.7$. The diagonal band structure and the high level of correlations along the ‘base’ of the ‘trident’ extending diagonally across the correlation matrix at small velocity lags result from correlations induced by the doublet nature of Mg II, which preferentially correlates velocity bins which probe the same underlying structures (see text for more details).

4.2 The Likelihood

Following standard practice for correlation function measurements, we adopt a multivariate Gaussian likelihood for the Mg II forest correlation function

$$L(\hat{\xi}(\Delta v) | [\text{Mg}/\text{H}], \langle x_{\text{H I}} \rangle) = \frac{1}{\sqrt{(2\pi)^k \det \mathbf{C}}} \exp\left(-\frac{1}{2} \mathbf{d}^T \mathbf{C}^{-1} \mathbf{d}\right), \quad (12)$$

where \mathbf{C} is the covariance matrix and $\mathbf{d} \equiv \hat{\xi}(\Delta v) - \xi(\Delta v | [\text{Mg}/\text{H}], \langle x_{\text{H I}} \rangle)$, where $\hat{\xi}(\Delta v)$ is the correlation function estimated from the data and $\xi(\Delta v | [\text{Mg}/\text{H}], \langle x_{\text{H I}} \rangle)$ is the parameter dependent model correlation function, which we will henceforth simply denote by $\xi(\Delta v)$. We compute the correlation function in $k = 31$ linearly spaced velocity bins of equal width, which determines the dimensionality of \mathbf{d} and \mathbf{C} . We choose the bin width to match our resolution of 100 km s^{-1} , and the bin centers extend from velocity lags 80 km s^{-1} to 3080 km s^{-1} . From our ensemble of 10,000 skewers we compute the average value of $\xi(\Delta v)$ at each location on our 2D grid (51×201) of $\langle x_{\text{H I}} \rangle$ and $[\text{Mg}/\text{H}]$ models.

Typically the covariance matrix is either determined from the data itself, via i.e. a bootstrap procedure, or synthesized from forward models. Given the relatively small mock dataset that we consider $n_{\text{QSO}} = 10$ or $\Delta z_{\text{tot}} = 6.0$, the covariance estimated from the data would be too noisy so we adopt the latter approach. The covariance matrix is defined

⁹ For $\Delta z = 0.6$ and $z = 7.5$, we assume spectra covering the range $z = 6.9 - 7.5$ centered at $z_{\text{eff}} = 7.2$, such that velocity interval covered is $c\Delta z / (1 + z_{\text{eff}}) = 21,936 \text{ km s}^{-1}$

via

$$C_{ij} \equiv \langle [\hat{\xi}(\Delta v) - \xi(\Delta v)]_i [\hat{\xi}(\Delta v) - \xi(\Delta v)]_j \rangle \quad (13)$$

where the indices i and j denote bins of velocity lag Δv , and the angle brackets denote the average over an ensemble of mock realizations of the dataset in question, which in this case is a correlation function $\hat{\xi}(\Delta v)$ computed from a set of $n_{\text{path}} = 33$ skewers. Note that this covariance matrix depends on the model parameters ($\langle x_{\text{H I}} \rangle, [\text{Mg}/\text{H}]$). For each model in our 51×201 grid, we generate 10^6 mock datasets by grabbing $n_{\text{path}} = 33$ random skewers from our sample of 10,000 without replacement, and computing their average correlation function $\hat{\xi}(\Delta v)$, allowing us to estimate the covariance from eqn. (13).

A useful tool for visualizing the covariance structure is the correlation matrix defined by

$$\text{Corr}_{ij} \equiv \frac{C_{ij}}{\sqrt{C_{ii}C_{jj}}}. \quad (14)$$

Fig. 5 shows an example correlation matrix for a model with $\langle x_{\text{H I}} \rangle = 0.74$ and $[\text{Mg}/\text{H}] = -3.7$. The diagonal band structure of the correlation matrix can be easily understood. By definition the correlation matrix is unity along the diagonal. The other two prominent sidebands result from correlations induced by the doublet nature of Mg II, i.e. a fluctuation in $\xi(\Delta v)$ in a bin at $\Delta v = 1200 \text{ km s}^{-1}$ will preferentially correlate with fluctuations in velocity bins at $\Delta v = 1200 \pm 768 \text{ km s}^{-1}$. Finally, the steep rise of the correlation function towards zero-lag and its ‘mirror image’ at $\Delta v = 768 \text{ km s}^{-1}$ (see Fig. 3), implies correlation function estimates at small velocity lags correlate more strongly with each other. For example the correlation function bin at $\Delta v = 500 \text{ km s}^{-1}$, which is 268 km s^{-1} away from the doublet peak at $\Delta v = 768 \text{ km s}^{-1}$, actually contains contributions from the same structures producing the small-scale rise of the correlation function towards zero lag at velocity $\Delta v = 268 \text{ km s}^{-1}$, resulting in a high value for the correlation matrix ≈ 0.6 . These effects conspire to produce the high level of correlations along the ‘base’ of the ‘trident’ extending diagonally across the correlation matrix at small velocity lags.

Finally, we note that the ‘zero-lag’ $\xi(\Delta v)$ bin is completely omitted from our inference calculations. Although in principle this bin contains information, utilizing it would require that one subtract off the noise variance. Our 1σ noise level per spectral pixel is 1%, whereas the standard deviation of the Mg II forest per spectral pixel is 0.5% for a model with $\langle x_{\text{H I}} \rangle = 0.74$ and $[\text{Mg}/\text{H}] = -3.7$, and scales as roughly metallicity squared (see discussion in § 3.1). Thus using the ‘zero-lag’ bin would presume that one can determine the absolute noise level to exquisite accuracy, whereas using non-zero lags assumes that the noise correlations are much smaller than the signal correlations, which is a far weaker assumption given that the noise is expected to be white.

4.3 Results

Given our mock JWST dataset of $n_{\text{QSO}} = 10$ quasars (FWHM=100 km s^{-1} and S/N = 100, see § 2.6 and Fig. 2) we can use the likelihood in eqn. (12) to perform Markov Chain

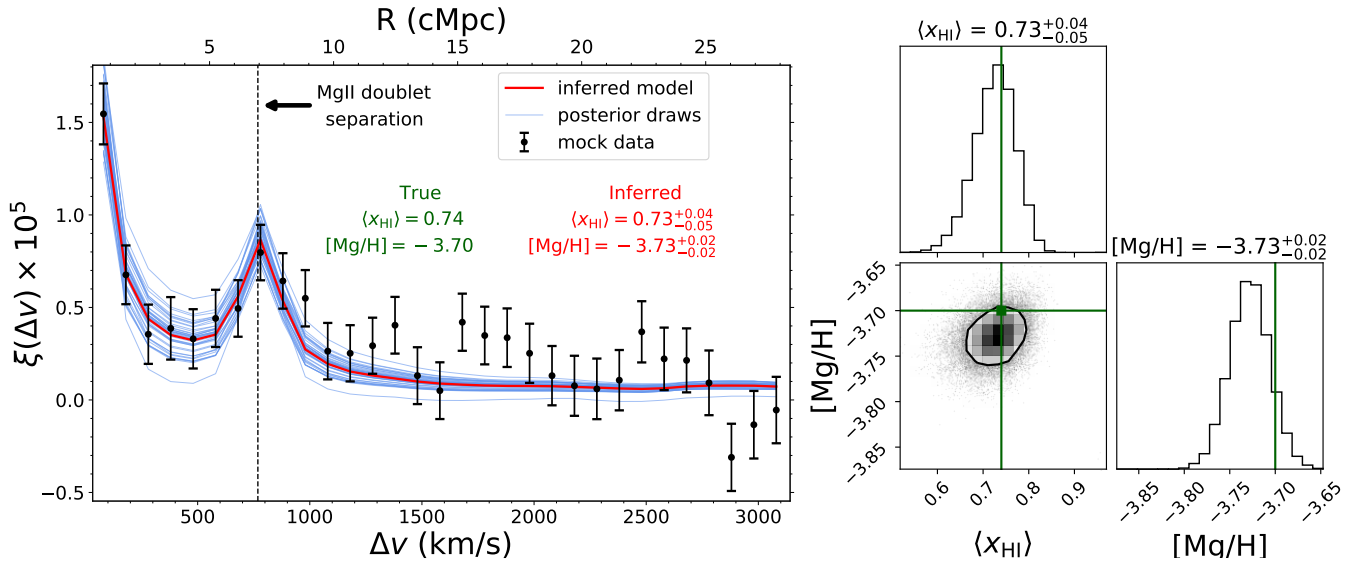


Figure 6. Simulated correlation function measurement and inference for a mock MgII forest dataset. *Left:* Points with error bars show the measured correlation function for a mock JWST dataset of $n_{\text{QSO}} = 10$ quasars (FWHM=100 km s⁻¹ and S/N = 100, see § 2.6 and Fig. 2) covering a total pathlength of $\Delta z_{\text{tot}} = 6.0$. The thin blue lines are random draws from the posterior sampled via MCMC (shown in the right panel), and the red curve is the mean inferred IGM model. *Right:* Corner plot determined via MCMC sampling of the posterior distribution. The true model had $[\text{Mg}/\text{H}] = -3.7$ and $\langle x_{\text{HI}} \rangle = 0.74$ as indicated by the dark green square and lines, whereas we recover values of $[\text{Mg}/\text{H}] = -3.73 \pm 0.02$ and $\langle x_{\text{HI}} \rangle = 0.73_{-0.05}^{+0.04}$, which are the median and 68% credible intervals of the marginalized posterior distributions for each parameter. At this location in parameter space we jointly determine the Mg abundance $[\text{Mg}/\text{H}]$ with a 1σ precision of 0.02 dex and measure the volume averaged neutral fraction $\langle x_{\text{HI}} \rangle$ to 5%.

Monte Carlo (MCMC) parameter inference. We assume a flat linear prior on the volume averaged neutral fraction extending from $x_{\text{HI}} = [0.0, 1.0]$, and a flat prior in the \log_{10} of the Mg abundance from $[\text{Mg}/\text{H}] = [-6.0, -2.0]$, i.e. our prior is uninformative and spans the parameter space covered by our model grid. For the fiducial model, we choose $[\text{Mg}/\text{H}] = -3.7$ and $x_{\text{HI}} = 0.74$, where the former is motivated by IGM metallicity measurements at lower- z , and the latter by current reionization constraints from the CMB (e.g. Planck et al. 2018), IGM damping wings towards $z \gtrsim 7$ quasars (Mortlock et al. 2011; Greig et al. 2017; Bañados et al. 2018; Davies et al. 2018b; Greig et al. 2019; Wang et al. 2020; Yang et al. 2020) and the disappearance of strong Ly α emission from galaxies (Mason et al. 2018, 2019; Hoag et al. 2019). The resulting mock correlation function and parameter constraints are shown in Fig. 6. Our analysis indicates that for this combination of model parameters one can simultaneously determine the Mg abundance $[\text{Mg}/\text{H}]$, with a 1σ precision of 0.02 dex, and measure the global neutral fraction $\langle x_{\text{HI}} \rangle$ to 5%.

The constraining power of the MgII correlation function, or more precisely the width and orientation of the contours in the $\langle x_{\text{HI}} \rangle$ - $[\text{Mg}/\text{H}]$ plane in the right panel of Fig. 6, are a strong function of the true value of the parameters. We illustrate this dependence in Fig. 7, which shows the resulting 68% and 95% confidence intervals (colored lines) at a grid of values for the true model (indicated by filled circles) in the $\langle x_{\text{HI}} \rangle$ - $[\text{Mg}/\text{H}]$ plane. For intermediate values of the neutral fraction $\langle x_{\text{HI}} \rangle \approx 0.5$ and Mg abundances $[\text{Mg}/\text{H}] \gtrsim -4$, there is no significant degeneracy between the two parameters. At low $\langle x_{\text{HI}} \rangle \lesssim 0.1$ and high $\langle x_{\text{HI}} \rangle \gtrsim 0.9$ neutral fractions a degeneracy between the parameters starts to emerge. This degenerate behavior can be qualitatively un-

derstood as follows. For $\langle x_{\text{HI}} \rangle \lesssim 0.1$, the steepening power law shape of the correlation function washes out the peaks arising from small-scale structure toward both zero-lag and the doublet separation (see Fig. 3), particularly at JWST resolution (FWHM = 100 km s⁻¹) where these peaks are smeared (see Fig. 4). In this regime the additional constraining power provided by these peaks is washed out, and the $[\text{Mg}/\text{H}]$ increases the roughly power-law correlation function amplitude, whereas $\langle x_{\text{HI}} \rangle$ alters its amplitude and slope, resulting in a degeneracy. The degeneracy at $\langle x_{\text{HI}} \rangle \gtrsim 0.9$ occurs for similar reasons. For these largely neutral models, the power-law behavior of the correlation (left panel of Fig. 3) due to the topology of reionization is suppressed, and all the signal is concentrated at small velocity lags and at the doublet separation. In this regime the naive degeneracy expected from the optical depth (see eqn. 5 and the discussion at the end of § 3.1) sets in, since the degenerate product of metallicity and neutral fraction determine the amplitude of fluctuations and hence the correlation function. This degeneracy is exacerbated by the fact that reionization occurs from the inside out, and at high values of $\langle x_{\text{HI}} \rangle$ the rare ionized patches will be co-spatial with the highest density gas. As a fully neutral Universe is approached $\langle x_{\text{HI}} \rangle \rightarrow 1$ these dense regions become neutral, and the amplitude of the correlation function will become hyper-sensitive to $\langle x_{\text{HI}} \rangle$ due to the outsize contribution of these dense regions to the fluctuations. Together we expect some degeneracy between $[\text{Mg}/\text{H}]$ and $\langle x_{\text{HI}} \rangle$ to emerge at high values $\langle x_{\text{HI}} \rangle \gtrsim 0.9$, and that a small change in $\langle x_{\text{HI}} \rangle$ can compensate for a relatively large change in $[\text{Mg}/\text{H}]$, which is exactly the behavior observed in Fig. 7.

It is conceivable that the neutral IGM is actually totally pristine, as would be the case if the metals produced

by the star-formation that drives reionization remain highly concentrated around the galaxies producing them. In this scenario, we would obtain a null detection of the Mg II forest correlation function even if the IGM were significantly neutral. Such a null detection would nevertheless provide an upper limit on the enrichment of the IGM during the EoR, providing an extremely interesting constraint on the enrichment history of the Universe. To quantify this, we assume that an independent constraint on the reionization history exists from other probes (e.g. CMB, IGM damping wings, Ly α disappearance in galaxies, or 21cm observations) such that $\langle x_{\text{HI}} \rangle > 0.5$ at $z = 7.5$. For our fiducial model we choose $[\text{Mg}/\text{H}] = -6.0$ (the lowest metallicity in our grid) and $x_{\text{HI}} = 0.74$, which results in a correlation function effectively consistent with zero. We perform statistical inference via MCMC as before, but now adjust the prior to have $\langle x_{\text{HI}} \rangle > 0.5$, and importantly, we adopt a *linear prior* on the Mg abundance to be in the range $10^{[\text{Mg}/\text{H}]} = [0.0, 1.0]$. The reasoning behind changing the abundance prior to be linear, as opposed to the \log_{10} prior adopted above, is that for a logarithmic prior, the resulting upper limit on $[\text{Mg}/\text{H}]$ would depend on the prior range adopted, whereas this is not the case with a linear prior. Marginalizing over the unknown neutral fraction with the MCMC samples, we find that a null correlation function detection from our mock dataset would place an upper limit on the Mg abundance of $[\text{Mg}/\text{H}] < -4.4$ at 95% confidence. This stringent limit is nearly 0.5 dex more sensitive than the most metal-poor Lyman Limit Systems (LLSs) and Damped Ly α Systems (DLAs) known (Fumagalli et al. 2011; Crighton et al. 2016; Cooke et al. 2017; Robert et al. 2019) and is in the realm of the alpha element abundances of the most metal-poor stars known (Frebel & Norris 2015). But whereas these metal-poor absorbers and stars constitute the rarest outliers from their respective parent populations, the sensitive Mg II forest abundance constraint one would obtain is the average for the IGM as a whole.

5 MODELING CIRCUMGALACTIC MG II ABSORBERS

Up to this point our analysis has ignored the impact of Mg II absorption line systems associated with galaxies. Specifically, our toy enrichment model assumes that all the gas in the Universe is suffused with Mg parameterized by a uniform abundance $[\text{Mg}/\text{H}]$. In reality, there will be a high concentration of Mg in the circumgalactic environs of galaxies, and it is important to understand how contamination from these CGM absorbers impacts the Mg II forest correlation function and our resulting parameter constraints.

We now expand our toy enrichment model to have two components, the uniform metallicity IGM that we considered previously plus additional CGM absorbers arising from galaxies. To model the latter, we must consider two quantities: their line density as a function of absorption line strength and the spatial distribution distribution of metal absorbers.

5.1 The Abundance of CGM Absorbers

To populate our simulated skewers with CGM absorbers we require the distribution function $\frac{d^2N}{dzdW_\lambda}$ of rest-frame

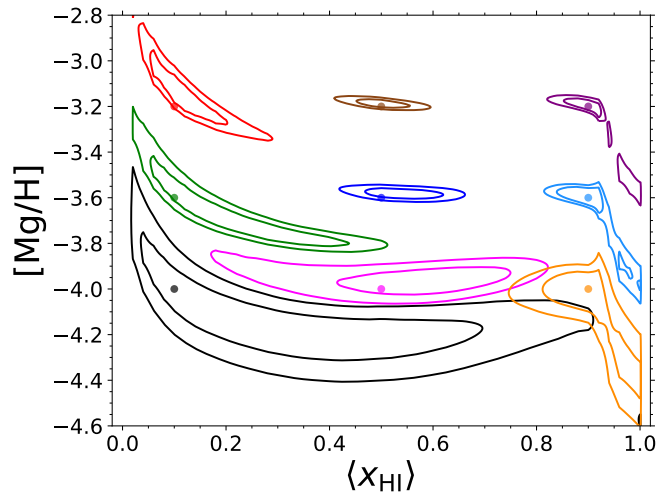


Figure 7. Constraining power of a mock Mg II forest dataset at different locations in parameter space. Contours indicate the 68% and 95% confidence regions resulting from a mock JWST dataset of $n_{\text{QSO}} = 10$ quasars (FWHM=100 km s $^{-1}$ and S/N = 100, see § 2.6 and Fig. 2) covering a total pathlength of $\Delta z_{\text{tot}} = 6.0$. The filled circles indicate the true value of the model from which the mock dataset was drawn, which were chosen on a grid of locations in the 2D parameter space at $[\text{Mg}/\text{H}] = [-3.2, -3.6, -4.0]$ and $\langle x_{\text{HI}} \rangle = [0.1, 0.5, 0.9]$.

equivalent width. Whereas studies sensitive to the strongest absorbers typically adopt an exponential form (e.g. Nestor et al. 2005; Chen et al. 2017) for this distribution function, echelle based searches sensitive enough to detect weak Mg II absorbers $W_\lambda \lesssim 0.1 \text{ \AA}$ find that a Schechter-like (Schechter 1976) function provides a better fit to the data (Kacprzak & Churchill 2011; Mathes et al. 2017),

$$\frac{d^2N}{dzdW_\lambda} = \frac{N_*}{W_*} \left(\frac{W_\lambda}{W_*} \right)^\alpha \exp\left(-\frac{W_\lambda}{W_*}\right), \quad (15)$$

which we will adopt here since, as we will see, only the weakest CGM absorbers are expected to significantly contaminate the Mg II forest signal arising from the neutral IGM.

The abundance of weak absorbers at $z > 6$ is currently not well constrained by observations. Chen et al. (2017) measured $\frac{d^2N}{dzdW_\lambda}$ from the redshift range $z = 6.0 - 7.08$ from a sample of high-redshift quasars, and Bosman et al. (2017) surveyed absorbers over nearly the same interval using a single high-quality spectrum of the ULAS J1120+0641 ($z_{\text{em}} = 7.08$) quasar sightline. These measurements are shown in Fig. 8. Note that they are not independent since the ULAS J1120+0641 quasar is also in the Chen et al. (2017) sample, although their spectrum is not as sensitive. Clearly current data are too noisy to independently constrain the three parameters (α, W_*, N_*) governing the equivalent width distribution in eqn. (15), as also emphasized by Bosman et al. (2017). We thus adopt the following approach to set their values. The most important parameter is the slope α , since it has the largest impact on the abundance of weak absorbers that dominate the contamination of the Mg II forest. Mathes et al. (2017) used a large archival echelle dataset to measure $\frac{d^2N}{dzdW_\lambda}$ for ($0.01 \text{ \AA} < W_\lambda < 10 \text{ \AA}$) over the redshift range $0.14 < z < 2.64$, and found slopes in the range $\alpha = -1.1$ to -0.8 . We thus adopt the value to $\alpha = -0.8$ consistent with

their measurement of $\alpha = -0.81 \pm 0.12$ in the highest redshift bin ($1.53 < z < 2.64$) that they studied. To set the other parameters, we simply fix $W_* = 1.0 \text{ \AA}$, and then we determine N_* by requiring that our equivalent width distribution reproduce the abundance of absorbers dN/dz in the range $0.6 \text{ \AA} < W_\lambda < 1.0 \text{ \AA}$ at $z = 7.5$. Specifically, Chen et al. (2017) fit the dN/dz with a functional form $dN/dz = A(1+z)^\beta$ with $A = 0.09$ and $\beta = 0.82$ (see their Table 7 and Figure 10) implying $dN/dz = 0.52$ at $z = 7.5$. This procedure finally yields $(\alpha, W_*, N_*) = (-0.80, 1.0 \text{ \AA}, 2.34)$ which gives the equivalent width distribution shown as the red curve in Fig. 8. We assume that CGM Mg II absorbers follow this distribution, but we truncate it at the low and high equivalent widths of $W_{\lambda, \text{min}} = 0.01 \text{ \AA}$ and $W_{\lambda, \text{max}} = 10 \text{ \AA}$, respectively, where these values correspond to roughly the weakest and strongest absorbers that have been observed to date (e.g. Mathes et al. 2017).

5.2 The Clustering of CGM Absorbers

Because of their higher abundance, most of what we know about the spatial distribution of metals in the IGM comes from C IV absorbers. Significant effort has been dedicated to understanding how strong C IV (i.e. $N_{\text{C IV}} \gtrsim 10^{13} \text{ cm}^{-2}$ or $W_\lambda \gtrsim 0.20 \text{ \AA}$) systems cluster, including both auto-correlation studies (Quashnock & Stein 1999; Coppolani et al. 2006; Martin et al. 2010), as well as cross-correlation analyses with both Lyman Break Galaxies (Adelberger et al. 2003, 2005) and quasars (Vikas et al. 2013; Prochaska et al. 2013). Similarly, the auto-correlation of strong Mg II absorbers (i.e. $W_\lambda \gtrsim 1.0 \text{ \AA}$) has been measured (Steidel & Sargent 1992; Quashnock & Vanden Berk 1998; Tytler et al. 2009) as well as the cross-correlation with so-called luminous red galaxies (LRGs; e.g. Bouché et al. 2006; Lundgren et al. 2009; Gauthier et al. 2014). The qualitative picture that emerges from these studies is that these strong absorbers are clustered similar to co-eval galaxies and reside in dark matter halos of $\sim 10^{12} M_\odot$. But as we will see, the strong absorbers that contaminate a Mg II forest measurement will be easy to identify and mask in the JWST spectra that we envision obtaining, and it is the weak absorption line systems that cannot be individually detected which will be our dominant contaminant.

Much less is known about the clustering of weak absorption systems, as these can only be identified in high S/N ratio echelle resolution spectra (e.g. Churchill et al. 1999; Songaila 2005; Narayanan et al. 2007; D’Odorico et al. 2010; Mathes et al. 2017; Mas-Ribas et al. 2018), and the relative paucity of such data inhibits the compilation of the large absorber samples required to measure weak clustering signals. The most comprehensive and sensitive study is the work by Boksenberg & Sargent (2015), who measured the clustering of weak C IV absorbers ($N \gtrsim 10^{12} \text{ cm}^{-2}$ or $W_\lambda \gtrsim 0.02 \text{ \AA}$) from a sample of ~ 200 systems over the redshift range $1.6 \lesssim z \lesssim 4.4$. They found significant clustering for $\Delta v \lesssim 300 \text{ km s}^{-1}$ ($r_\parallel = 2.7 \text{ cMpc}$ if it were in the Hubble flow), but clustering is not detected on larger scales. Furthermore, they argue rather convincingly that this small-scale clustering signal likely arises from the complex kinematics of individual C IV components, which can be grouped together into aggregate absorption ‘systems’, and that this signal arises primarily from the stronger absorbers in their sample.

Furthermore, after grouping these systems into aggregate systems the clustering signal measured is consistent with zero. These results are in qualitative agreement with previous work on weak C IV based on smaller samples (Sargent et al. 1980, 1988; Petitjean & Bergeron 1994; Rauch et al. 1996; Pichon et al. 2003, but see Scannapieco et al. (2006)) as well as an analogous analyses of weak Mg II absorbers ($W_\lambda \gtrsim 0.3 \text{ \AA}$; Petitjean & Bergeron 1990; Churchill et al. 2003). Given the lack of convincing evidence for $\gtrsim 1 \text{ cMpc}$ clustering of weak absorption line systems, we therefore neglect absorber clustering in our CGM model. This is a reasonable assumption because the clustering of the Mg II forest on large scales ($\Delta v \gtrsim 1000 \text{ km s}^{-1}$ or $r_\parallel \gtrsim 9 \text{ cMpc}$) results from large coherent fluctuations in the IGM neutral fraction, which should dominate over any weak large scale clustering of CGM absorbers.

5.3 The Final CGM Model

We populate our simulated Mg II forest spectra with CGM contaminants by drawing a number of absorbers from the equivalent width distribution shown in Fig. 8 commensurate with the pathlength Δz probed by the skewer. Each absorber is randomly assigned a velocity along the skewer, consistent with our assumption of no absorber clustering. The optical depth of each absorber is added to the skewer using the full Voigt profile for an assumed Gaussian velocity distribution. This requires a recipe for choosing a $N_{\text{Mg II}}$ and b -value that gives the desired rest-frame equivalent width W_λ . On the linear part of the curve-of-growth (COG) the relationship between $N_{\text{Mg II}}$ and W_λ is

$$W_\lambda = 0.43 \text{ \AA} \left(\frac{N_{\text{Mg II}}}{10^{13} \text{ cm}^{-2}} \right), \quad (16)$$

and the optical depth at line center for the Gaussian core of the Voigt profile is

$$\tau_0 = 1.3 \left(\frac{N_{\text{Mg II}}}{10^{13} \text{ cm}^{-2}} \right) \left(\frac{b}{20 \text{ km s}^{-1}} \right)^{-1}, \quad (17)$$

For weak Mg II absorbers $W_\lambda \lesssim 0.1 \text{ \AA}$ the optical depth weighted second moments are typically $\sim 20 \text{ km s}^{-1}$, whereas strong absorbers with $W_\lambda > 1 \text{ \AA}$ are significantly broader $\sim 100 \text{ km s}^{-1}$ (Churchill & Vogt 2001; Mathes et al. 2017). According to eqns. (16) and (17), the COG saturates around $N_{\text{Mg II}} = 10^{13} \text{ cm}^{-2}$ or a $W_\lambda \approx 0.4 \text{ \AA}$ for $b = 20 \text{ km s}^{-1}$. Thus, it will be impossible to generate the strongest absorbers $W_\lambda > 1 \text{ \AA}$ with such a low b -value. To model changes in b for stronger absorbers, we adopt

$$b = b_{\text{weak}} + (b_{\text{strong}} - b_{\text{weak}}) \times \left[1 + \exp \left(- \frac{\log_{10} N_{\text{Mg II}} - \log_{10} N_{\text{strong}}}{\Delta \log_{10} N} \right) \right]^{-1}, \quad (18)$$

where the second term is the ‘logistic sigmoid’ function that guarantees a smooth transition with column density between the value of b_{weak} and b_{strong} around the transition column density $\log_{10} N_{\text{strong}}$, over a column density interval set by $\Delta \log_{10} N$. We adopt $b_{\text{weak}} = 20 \text{ km s}^{-1}$, $b_{\text{strong}} = 200 \text{ km s}^{-1}$, $\log_{10} N_{\text{strong}} = 16$ and $\Delta \log_{10} N = 0.25$, where all column densities are in units of cm^{-2} . We will see that the contamination of the IGMs Mg II forest signal is insensitive to the strongest

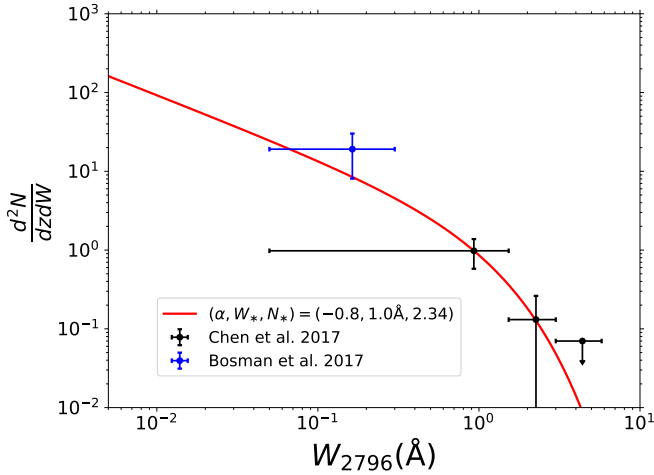


Figure 8. Rest-frame equivalent width distribution for CGM Mg II Absorbers. The red curve shows the Schechter function model (see eqn. (15)) used for the distribution of CGM equivalent widths. The black and blue points are measurements probing the redshift range $6.0 \lesssim z \lesssim 7.08$ from Chen et al. (2017) and Bosman et al. (2017), respectively.

absorbers, which are easily identified and masked, and is instead dominated by the weaker absorbers below the detection limit of our simulated spectra, which is $W_\lambda \approx 0.04 \text{ \AA}$ or $N_{\text{Mg II}} \approx 10^{12} \text{ cm}^{-2}$ for the mock JWST spectra. These weak absorbers have $b \approx 20 \text{ km s}^{-1}$ much smaller than the resolution of the JWST spectra (FWHM=100 km s^{-1}) that we simulate. For these reasons our results are insensitive to the details of the b values assumed: the weak absorbers are not resolved by our spectra and the strong absorbers are masked.

6 THE FLUX PROBABILITY DISTRIBUTION FUNCTION OF THE MG II FOREST

The goal of this section is to understand the contamination of the IGM Mg II forest absorption by CGM absorption arising from the enriched halos of galaxies. To do so we must quantify, for a given absorption level, the likelihood that it arises from the IGM versus the CGM. Our modeling of CGM absorbers focused on the distribution of rest-frame equivalent widths, W_λ , which is the obvious choice for measurements of discrete Mg II absorbers, particularly in the regime where they are not spectrally resolved. But the notion of equivalent width loses its utility for a continuous absorption field, analogous to the situation for the Ly α forest at lower redshift. In this regime, choosing the spectral regions for the equivalent width integral would be arbitrary – it is impossible to decide where the absorption starts and ends. Indeed, the more appropriate description of a continuous random field is the flux PDF, which will be the focus of this section.

The equivalent width distribution and the flux probability distribution are however related to each other. Recall the definition of equivalent width

$$W_\lambda = \int (1 - F) d\lambda. \quad (19)$$

Defining the limits of integration to simply be the bound-

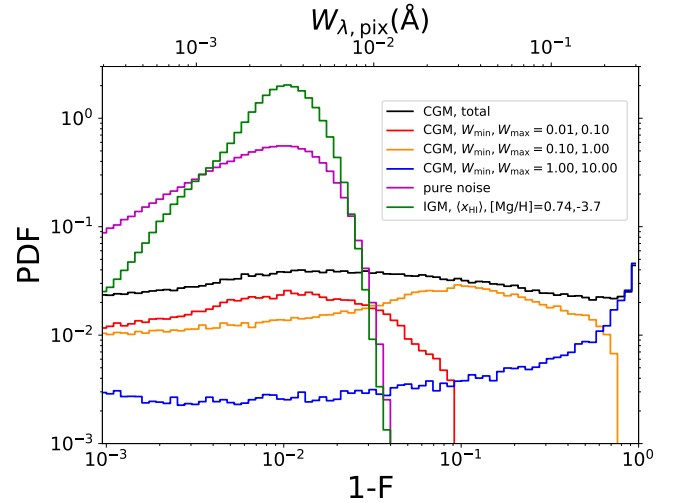


Figure 9. Flux PDF resulting from CGM absorbers compared to that of the IGM. The black histogram shows the PDF resulting from the entire population of CGM absorbers that we add to our spectra, whereas the red, yellow, and blue histograms show the contributions from each decade of W_λ to the total CGM PDF. For comparison, the green histogram shows the PDF resulting from pure IGM Mg II forest absorption for our fiducial model ($\langle x_{\text{H I}} \rangle, [\text{Mg}/\text{H}] = (0.74, -3.7)$). Noise has not been added to the spectra used to construct these PDFs, but for comparison, the magenta histogram shows the PDF for pure Gaussian noise ($S/N = 100$). The counterintuitive appearance of these PDFs arises from the logarithmic scale and because we show only the positive fluctuations.

aries of a pixel in our spectrum gives rise to the concept of a pixel equivalent width $W_{\lambda, \text{pix}} \equiv (1 - F)\Delta\lambda$, where $\Delta\lambda$ is the rest-frame width of a spectral pixel, which is 0.31 \AA for the JWST spectra that we model here. Note that unlike the conventional definition of equivalent width, the pixel equivalent width does depend on the spectral resolution if the ‘pixel’ size is chosen to be smaller than the resolution element of the spectrograph.

Consequently, we want to study the probability distribution of $1 - F$, which is linearly related to the distribution of $W_{\lambda, \text{pix}}$. Given the large dynamic range of approximately three decades in W_λ (see Fig. 8) that we model and the high $S/N = 100$ of the mock spectra, it is preferable to work with $\log_{10}(1 - F)$. We thus define our PDF as

$$\int_a^b \frac{dP}{d \log_{10}(1 - F)} d \log_{10}(1 - F) = \text{frac}(a, b) \quad (20)$$

where $\text{frac}(a, b)$ is the fraction of the total pixels lying in the interval $\{a, b\}$.

In Fig. 9 we compare the flux PDF resulting from CGM absorbers with that arising from the IGM and noise. These PDFs are computed from our simulated IGM (see § 2) and CGM skewers (see § 5), respectively. Specifically, the green histogram shows pure IGM Mg II forest absorption for our fiducial model ($\langle x_{\text{H I}} \rangle, [\text{Mg}/\text{H}] = (0.74, -3.7)$ with no CGM contamination, whereas the black histogram shows the same skewer pathlength populated only by CGM absorbers. Noise has not been added to the spectra used to construct these PDFs, but for comparison, the magenta histogram in Fig. 9 shows the PDF for pure Gaussian noise ($S/N = 100$). The counterintuitive appearance of these PDFs arises from the

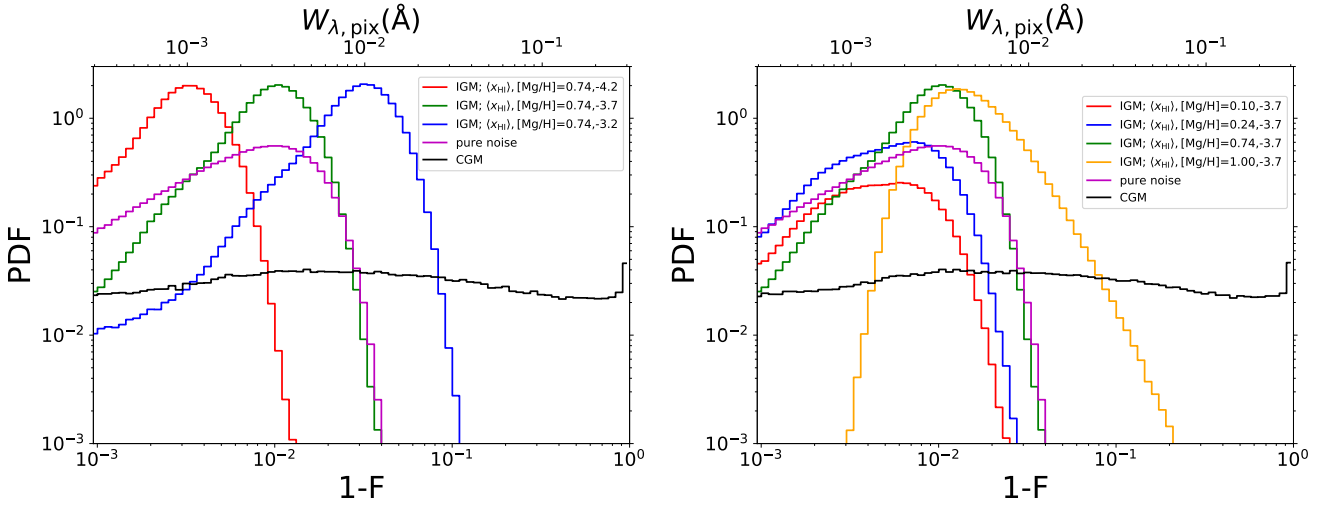


Figure 10. Dependence of IGM flux PDF on model parameters compared to that of the CGM. *Left:* Red, green, and blue histograms show the effect of changing $[\text{Mg}/\text{H}]$ at fixed $\langle x_{\text{H I}} \rangle = 0.74$. For comparison the black histogram shows the PDF resulting from CGM absorbers. Noise has not been added to the spectra used to construct these PDFs, but the magenta histogram shows the PDF for pure Gaussian noise ($S/N = 100$). *Right:* Red, blue, green, and orange histograms show the effect of changing $\langle x_{\text{H I}} \rangle$ at fixed $[\text{Mg}/\text{H}] = -3.7$. Black and magenta histograms are the same as in the left panel.

logarithmic scale and because we show only the positive fluctuations. The other colored histograms illustrate the contribution of CGM absorbers within a given decade of W_λ to the total CGM PDF (shown in black). The cutoffs at large values of $1 - F$ (W_λ) in these decade-specific PDFs can be easily understood. For example, the strongest absorbers in the range $(W_{\min}, W_{\max}) = (0.01 \text{ \AA}, 0.1 \text{ \AA})$ will be at the upper edge of the bin $W_\lambda \approx 0.1 \text{ \AA}$. For such an absorber the highest value of $1 - F \approx 0.1$ ($W_{\lambda, \text{pix}} \approx (1 - F)\Delta\lambda = 0.1 \times 0.31 \text{ \AA} = 0.03 \text{ \AA}$). In other words, the most absorbed pixel contributes about one third of the total W_λ , which is the integral over the full absorption profile in eqn. (19). The flat PDF shape at smaller values of $1 - F$ results from both the range of W_λ considered in each decadal bin, as well as very weak absorption imprinted on a large number of pixels by the Gaussian wings of the spectrograph line spread function. Finally, the contribution from each decade of W_λ to the final CGM PDF (black), that is the relative normalization of each histogram, results from the shape of the equivalent width distribution, $\frac{d^2 N}{dz dW_\lambda}$ (see Fig. 8).

The shape and amplitude of the IGM PDF, and thus relative importance of noise and CGM contamination, depend on the structure of the Mg II forest as parameterized by $\langle x_{\text{H I}} \rangle$ and $[\text{Mg}/\text{H}]$. The left panel of Fig. 10 shows that increasing the Mg abundance at a fixed volume averaged neutral fraction ($\langle x_{\text{H I}} \rangle = 0.74$) simply shifts the PDF to the right. This is intuitive – because the Mg II forest optical depth depends linearly on metallicity (see eqn. (6)), and in the low optical depth limit $1 - F \approx \tau \propto Z$, and thus a change in metallicity amounts to a simple rescaling of $1 - F$, as is apparent in the left panel of Fig. 10. Changing $\langle x_{\text{H I}} \rangle$ at fixed $[\text{Mg}/\text{H}]$ produces more complex changes in PDF shape, as illustrated in the right panel of Fig. 10. As compared to a model with $(\langle x_{\text{H I}} \rangle, [\text{Mg}/\text{H}]) = (1.0, -3.7)$ (orange), a lower $\langle x_{\text{H I}} \rangle = 0.1$ (red) reduces the abundance of percent level $1 - F$ fluctuations by about an order of magnitude, which is the naive expectation given the order of magnitude change in volume filling factor. But low values of $\langle x_{\text{H I}} \rangle \lesssim 0.3$ also flatten out

the peak in the PDF and shift it to lower $1 - F$ values, as is apparent for the $\langle x_{\text{H I}} \rangle = 0.1$ (red) and $\langle x_{\text{H I}} \rangle = 0.24$ (blue) histograms in Fig. 10.

In summary, for our fiducial IGM model $(\langle x_{\text{H I}} \rangle, [\text{Mg}/\text{H}]) = (0.74, -3.7)$ (green histograms in Figs. 9 and 10), the Mg II forest produces a distribution of $1 - F$ fluctuations peaking around a percent, which are a factor of about four more abundant than noise fluctuations at our assumed $S/N = 100$. CGM absorbers produce a flat distribution of $1 - F$ fluctuations, which are almost two orders of magnitude less abundant than IGM fluctuations for $1 - F \approx 0.01$, but which overwhelmingly dominate at $1 - F \gtrsim 0.03$, where both IGM fluctuations and noise fluctuations are exponentially suppressed. As the parameters governing the IGM are varied (see Fig. 10), the $1 - F$ value at which the IGM PDF peaks shifts, as does the location of the exponential cutoff at high $1 - F$. However, qualitatively the picture is unchanged. At the $1 - F$ values where the IGM PDF peaks, it exceeds the flat CGM PDF by at least an order of magnitude for the majority of IGM parameter space. This indicates that CGM absorbers can simply be identified and masked without significantly modifying the distribution of IGM fluctuations, and hence preserving the information about enrichment and reionization encoded in the Mg II forest.

7 IDENTIFYING AND MASKING CGM ABSORPTION

We now present a procedure for filtering out the CGM contamination by identifying and masking pixels impacted by CGM absorption. We first focus attention on our fiducial IGM model $(\langle x_{\text{H I}} \rangle, [\text{Mg}/\text{H}]) = (0.74, -3.7)$, and later describe how our results generalize to other Mg II forest models. To identify the location of CGM absorbers, we follow standard practice (e.g. Zhu & Ménard 2013; Chen et al. 2017) and convolve our noisy mock spectra with a matched filter, $W(v)$ corresponding to the transmission profile of a Mg II doublet.

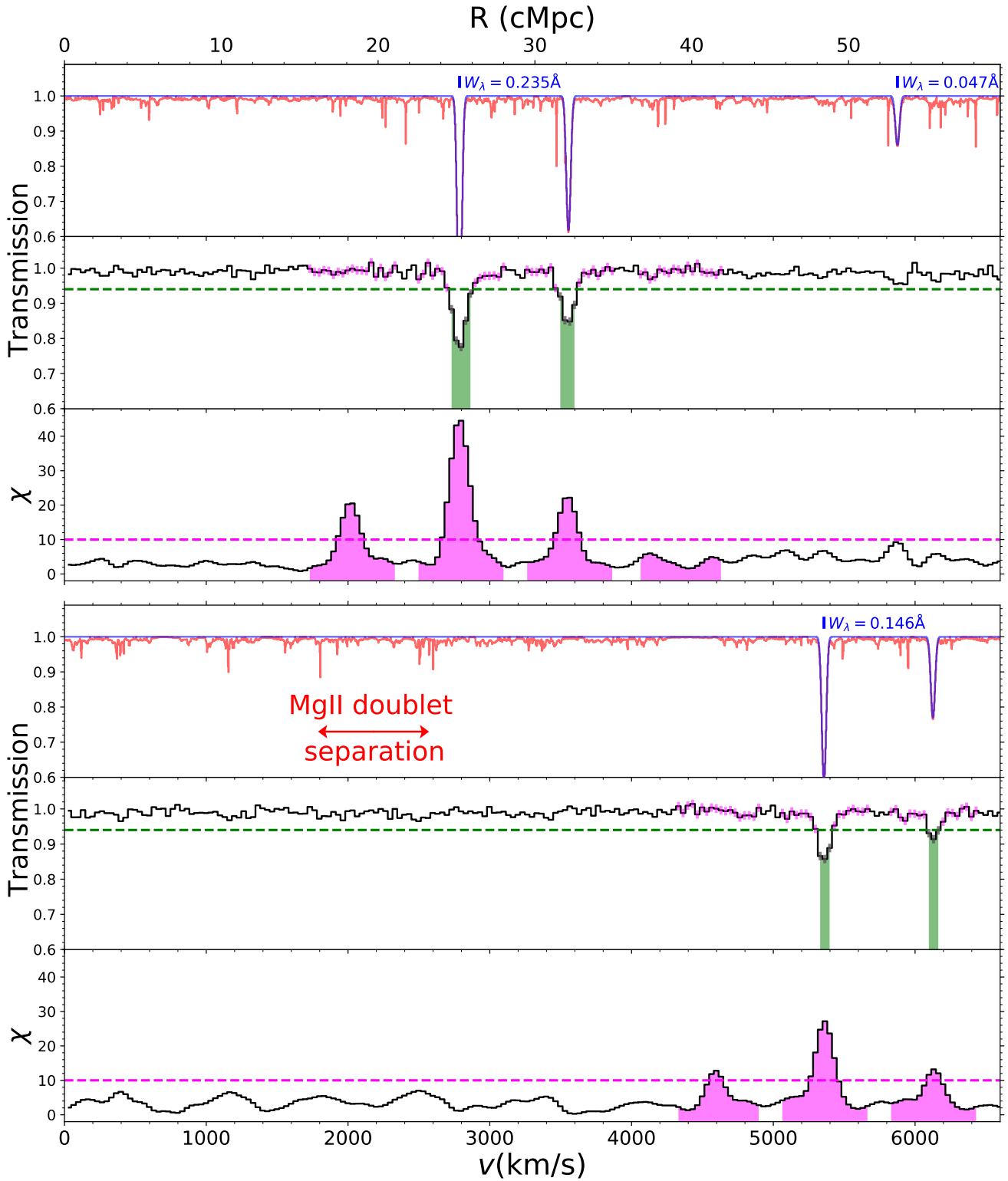


Figure 11. Illustration of our procedure for masking CGM absorbers. The two sets of three panel figures (top and bottom) show simulated Mg II forest spectra of the IGM contaminated by CGM absorbers for two absorption skewers. *Top Panels:* The perfect input spectra (IGM in red, CGM in blue), with the individual CGM absorbers labeled by their rest-frame equivalent width W_λ . *Middle Panels:* Forward modeled JWST spectra with resolution $\text{FWHM} = 100 \text{ km s}^{-1}$ and $\text{S/N} = 100$. Vertical rectangles indicate pixels that have been masked by our ‘flux-filtering’ (green), ‘ χ -filtering’ (magenta), or are masked by both ‘flux + χ -filtering’ (gray). The horizontal green dashed line at $F = 0.94$ ($1 - F = 0.06$) indicates the ‘flux-filtering’ threshold (see left panel of Fig. 12), and the green shaded region indicates spectral regions below the threshold (above the $1 - F$ threshold) that are masked. *Lower Panels:* Spectrum of $\chi(v)$ (see eqn. 21) computed from the JWST mock spectra in the middle panels. Note the triple-peak structure, which naturally arises from convolving an absorption doublet with a doublet matched-filter due to aliasing when the data/filter overlap with the opposite member of the doublet. The magenta dashed line at $\chi = 10$ indicates the ‘ χ -filtering’ threshold (see right panel of Fig. 12). Pixels above this threshold are all masked, and we also mask a $\pm 300 \text{ km s}^{-1}$ window around any peak identified that has $\chi > 10$, as well as at locations $+v_{\text{MgII}}$ away to account for the redder member of the doublet. We conservatively do not attempt to distinguish between real and aliased peaks. The magenta shaded regions indicate the regions that are masked by this ‘ χ -filtering’.

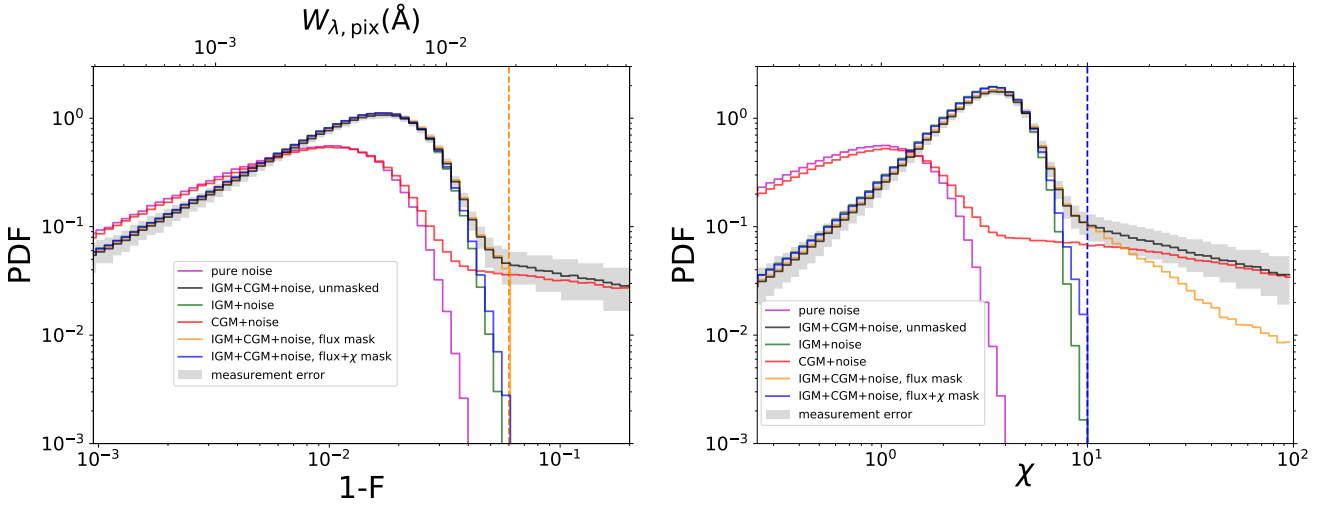


Figure 12. Impact of filtering on the flux and significance PDFs. *Left:* The black histogram shows the PDF of $1 - F$ for spectra which include the IGM Mg II forest and CGM contamination with noise now added. The colored histograms show the PDFs for various combinations of subcomponents: IGM + noise (green), CGM + noise (red), and pure noise (magenta). The impact of ‘flux-filtering’ on the PDF, whereby all pixels with $1 - F > 0.06$ (vertical orange dashed line) are masked is illustrated by the orange histogram. The blue histogram shows the combination of this ‘flux-filtering’ and ‘ χ -filtering’, whereby pixels with $\chi > 10$ are also masked (see right). *Right:* Same as left panel but now showing the PDF of the significance field χ (see eqn. (21) and Fig. 11). The orange histogram now shows the impact of ‘flux-filtering’ on the χ PDF, whereas blue shows the combination of ‘flux + χ -filtering’ with $\chi > 10$ (vertical blue dashed line).

Extrema in this filtered field are identified as potential absorber locations. We define the significance field

$$\chi(v) \equiv \frac{\int [1 - F(v')] W(|v - v'|) dv'}{\sqrt{\int \sigma_F^2(v') W^2(|v - v'|) dv'}}, \quad (21)$$

where σ_F^2 is the variance of $1 - F$ resulting from the spectrograph noise. As defined, χ is essentially a S/N ratio, with the signal being the matched filtered field, and the noise the one sigma fluctuation of the filtered field that would arise from noise fluctuations alone. For $W(v)$ we use $1 - e^{-\tau(v)}$, where $\tau(v)$ is the Voigt profile describing a Mg II doublet with a Gaussian velocity distribution, assuming a column density of $N_{\text{Mg II}} = 10^{13.5} \text{ cm}^{-2}$ and Doppler parameter $b = \sqrt{2} \times \text{FWHM}/2.35 = 60.2 \text{ km s}^{-1}$, where $\text{FWHM} = 100 \text{ km s}^{-1}$ is the resolution of our mock JWST spectra. This choice for b is sensible because the Doppler parameters of weak absorbers $b = 20 \text{ km s}^{-1}$ (see § 5) are not resolved by our spectral resolution. Since this combination of b and $N_{\text{Mg II}}$ puts us on the linear part of the COG (see eqn. 16) $W(v) = 1 - e^{-\tau(v)} \propto N_{\text{Mg II}}$ and thus this normalization simply cancels out of our definition of χ in eqn. (21).

Fig. 11 shows simulated Mg II forest spectra of the IGM contaminated by CGM absorbers for two absorption skewers (i.e. top three and bottom three panels). The upper panel of each plot shows the perfect input spectra (IGM in red, CGM in blue), whereas the middle panels show forward modeled JWST spectra with finite resolution and S/N. The lower panels show $\chi(v)$ computed from these JWST spectra. Notice that because $W(v)$ has a double Gaussian shape with the two peaks separated by the Mg II doublet separation $v_{\text{Mg II}}$, the χ spectrum of an absorber exhibits a triple-peak structure with one peak at the true location of the absorber and two ‘aliased’ peaks at $\pm v_{\text{Mg II}}$. This aliasing is unavoidable and results when the $\lambda 2796$ or $\lambda 2804$ part of the filter overlaps with the opposite member of the doublet in the data.

We implement two distinct filtering procedures by simply masking spectral regions that are likely to be contaminated by the CGM. The left panel of Fig. 12 shows the PDF of $1 - F$, analogous to those shown Figs. 9 and 10, but where we have now added noise to the skewers, as illustrated in the middle panels of Fig. 11. The black histogram in Fig. 12 shows the full PDF of the Mg II forest plus CGM contamination, whereas the colored histograms show PDFs of combinations of subcomponents. In particular, the green histogram shows that, for our fiducial IGM model plus noise, fluctuations with $1 - F > 0.06$ (orange dashed vertical line) lie beyond the exponential cutoff of the IGM PDF. All of these large fluctuations are caused by CGM absorption (red histogram). This motivates our ‘flux-filtering’ masking procedure, whereby pixels with $1 - F > 0.06$ are simply masked, corresponding to the shaded green regions in Fig. 11.

An effective filtering procedure should result in a flux PDF as close to the pure IGM (green histogram) in the left panel of Fig. 12 as possible. There it is seen that ‘flux-filtering’ simply truncates the PDF (orange histogram) above the $1 - F = 0.06$ threshold (orange vertical dashed line), but still leaves an appreciable number of CGM contaminating pixels just below it. The middle panels of Fig. 11 show that these pixels can be identified with the wings of CGM absorbers lying just above the $F = 0.94$ (below the $1 - F = 0.06$) threshold (green horizontal dashed line). Setting the threshold to a lower value of $1 - F$ would mask them, but at the expense of suppressing real IGM signal at $1 - F$ values where the IGM and CGM PDFs overlap. Instead, we need to identify the CGM absorbers and ‘grow’ our mask, which motivates a second masking procedure, which we refer to as ‘flux + χ -filtering’. The right panel of Fig. 12 shows the PDF of the χ field (see e.g. middle panels of Fig. 11) for the same combinations of subcomponents as the left panel. Analogous to $1 - F$, one observes that IGM fluctuations (green histogram) with $\chi \gtrsim 10$ are exponentially suppressed, and

that all of these high- χ pixels are due to CGM contamination (red histogram). We thus search for extrema in the χ field with $\chi > 10$, and mask a $\pm 300 \text{ km s}^{-1}$ region around each of these peaks at the peak location, as well as at locations $+v_{\text{Mg II}}$ away. Our peak finding is thus conservative: we mask a 600 km s^{-1} wide window to ensure we completely mask all the CGM absorption and we do not attempt to distinguish between real and aliased peaks.

What we will refer to as ‘ χ -filtering’ is the OR of three distinct boolean bad-pixel masks, i.e. where **True** corresponds to a pixel that will be masked in the correlation function computation. That is

$$\text{CHI_MASK} = \chi > 10 \text{ OR } \text{PEAK}_{2796} \text{ OR } \text{PEAK}_{2804}, \quad (22)$$

where PEAK_{2796} and PEAK_{2804} are the masked regions associated with each peak, and the location $+v_{\text{Mg II}}$ away, respectively. This mask is illustrated by the magenta shaded regions in the lower panels of Fig. 11. The final bad-pixel mask for ‘flux $+\chi$ -filtering’ is then

$$\text{FLUX_CHI_MASK} = 1 - F > 0.06 \text{ OR } \text{CHI_MASK}, \quad (23)$$

which is depicted by the vertical bars on the spectra in the middle panels of Fig. 11. After applying our total flux $+\chi$ -filtering masks to the entire ensemble of 10,000 skewers for our fiducial model, we are left with 77% of the pixels being unmasked, indicating that while our conservative masking does reduce the total pathlength, the reduction is not severe. The PDFs of $1 - F$ and χ for the ‘flux $+\chi$ -filtered’ spectra are shown as the blue histograms in the left and right panels of Fig. 12, respectively. That these PDFs very closely match those for pure IGM plus noise (green histograms) strongly suggests that we have achieved our goal of masking the majority of the CGM contaminated pixels.

The ultimate validation of this hypothesis comes from the clustering properties, which formed the basis for our parameter constraints on reionization and IGM enrichment (see Figs. 6 and 7). The impact of CGM contamination and masking on the correlation function is shown in Fig. 13. The black curve shows the correlation function $\xi(\Delta v)$ of the CGM contaminated Mg II forest without masking, which overwhelms the pure IGM signal by over two orders of magnitude (note the black curve is scaled down by a factor of 100). Nevertheless, our ‘flux $+\chi$ -filtering’ procedure successfully masks nearly all of the CGM absorption, and Fig. 13 shows that the resulting clustering signal (blue curve) is virtually indistinguishable from that of the pure IGM (green curve), especially in relation to the expected measurement errors for our fiducial JWST dataset (blue shaded bands).

The outsize influence of CGM absorbers on the Mg II forest may seem counterintuitive given one’s experience with the H I Ly α forest, where CGM absorbers, i.e. Lyman limit systems and damped Ly α absorbers, have a small impact on the correlation function and power spectrum (McDonald et al. 2005a; Rogers et al. 2018). There are two explanations for this difference. First, metals are far more abundant in the CGM than they are in the IGM, enhancing the impact of CGM contamination on their clustering signal compared to hydrogen. For example, our fiducial model assumes the IGM is enriched to $[\text{Mg}/\text{H}] = -3.7$, whereas we know that CGM absorbers at $z \sim 2-4$ have metallicities orders of magnitude higher spanning the range $-2 \lesssim \log_{10} Z \lesssim -1$ (Fumagalli et al. 2016). This large relative enhancement of metals in the

CGM vs IGM also likely holds at $z \sim 7$. Second, IGM absorbers in the $z \sim 2-4$ H I Ly α forest ($N_{\text{H I}} \sim 10^{12}-10^{14} \text{ cm}^{-2}$) are on the linear part of the COG, whereas the most abundant CGM absorbers have $N_{\text{H I}} \sim 10^{15}-10^{18} \text{ cm}^{-2}$. Thus they lie on the saturated part of the COG limiting their spectral imprint. This is however not the case for Mg II where a large population of CGM contaminants with $W_{\lambda} \lesssim 0.4$ lie on the linear part of the COG (see eqn. 16). These absorbers completely dominate the PDF of $1 - F$ for fluctuations greater than a few percent (see left panel of Fig. 10) and, if left unmasked, swamp the IGM clustering signal. To build further intuition about why the CGM absorber matter so much it helps to compare their mean flux decrement to that resulting from IGM metals. For the CGM model implemented here, we find that for simulated skewers populated only with CGM absorbers $1 - \langle F \rangle = 0.0115$, which is slightly larger than the value for pure IGM skewers of $1 - \langle F \rangle = 0.00969$ with $(\langle x_{\text{H I}} \rangle, [\text{Mg}/\text{H}]) = (1.0, -3.7)$. This can be contrasted with the H I Ly α forest at $z \approx 3$ where optically thick absorbers with $N_{\text{H I}} > 10^{17.2} \text{ cm}^{-2}$ contribute a negligible amount of transmission $1 - \langle F \rangle \approx 0.01$ when compared to the mean transmission of $1 - \langle F \rangle = 0.67$ from the lower column density Ly α forest (Becker et al. 2013). But it still not immediately obvious why CGM absorbers yield a correlation function more than two orders of magnitude larger than the IGM Mg II forest (see Fig. 13) given that they contribute comparably to the IGM in the flux decrement. This outsize effect results from the fact that the strongest CGM absorbers, although rare, contribute $1 - F \gtrsim 0.5$ nearly two orders of magnitude larger than the typical decrement $1 - F \approx 0.01$ of IGM absorbers (see e.g. Fig. 10), and the correlation function is sensitive to the square of this enhanced absorption (see eqn. 11).

While we have shown that we can effectively suppress the impact of CGM absorbers on the correlation function for our fiducial model, our masking procedure involves choosing two thresholds: one for $1 - F$ which we took to be 0.06 and another for χ chosen to be 10. These thresholds were chosen to be just beyond the exponential cutoffs in the pure IGM + noise PDFs in Fig. 12, which prevents overly aggressive masking that could suppress some of the real IGM Mg II forest signal and yield biased parameter estimates. At face value, given that the choice of these thresholds depends on the expected fluctuations for a given model, our masking procedure appears to be model dependent. However, we argue that this actually is not the case, since the location of these thresholds can be determined by simply inspecting the PDFs in Fig. 12 for the real data. The gray shaded regions in the left and right panels show the expected 1σ measurement error on the $1 - F$ and χ PDFs respectively, for a mock JWST dataset. Guided by the generic expectation, elucidated in Figs. 9, 10 and 12, that the IGM PDF will peak at a characteristic value and sharply cutoff towards higher $1 - F$ (or χ), whereas the CGM PDF will be flat at these large $1 - F$ (χ), the masking thresholds can be chosen by simply inspecting the $1 - F$ and χ PDFs estimated from the data, and the relative size of the shaded error bars indicate that one would have ample signal-to-noise on these PDFs to do so.

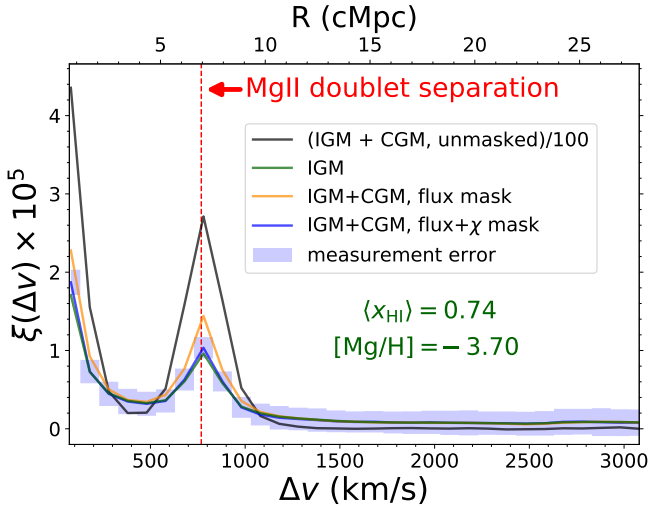


Figure 13. Impact of CGM absorbers on MgII Forest correlation function before and after filtering. The black curve shows the correlation function divided by 100 for skewers where CGM absorber contamination has been added to the IGM MgII forest. For comparison, the green curve shows the MgII forest correlation function for the uncontaminated IGM alone. The MgII forest model shown here has $(\langle x_{\text{HI}} \rangle, [\text{Mg}/\text{H}]) = (0.74, -3.7)$. The orange line shows that ‘flux-filtering’ greatly suppresses CGM contamination resulting in a correlation function very close to the IGM alone (green). Even better is the combination of ‘flux + χ -filtering’ shown as the blue curve, which results in a correlation function that is virtually indistinguishable from the pure IGM signal (green) relative to the expected 1σ errors (blue shaded regions) on the correlation function for our fiducial JWST dataset.

8 SUMMARY AND CONCLUSIONS

We proposed a novel experiment to detect the weak forest of low-ionization MgII absorbers in quasar spectra that will be present if the IGM is both significantly neutral and sufficiently enriched with metals. In contrast to the traditional approach of searching for discrete absorption systems, we advocated treating this forest of metal absorption as a continuous cosmological random field and measuring its two-point correlation function and PDF, leveraging techniques from precision cosmology. To quantify the efficacy of approach method, we simulated the MgII forest for the first time by combining a large cosmological hydrodynamical simulation of the pre-reionization IGM with a semi-numerical computation of the global reionization topology, assuming a simple enrichment model where the IGM is uniformly suffused with metals. We studied the behavior of the MgII forest correlation function, $\xi(\Delta v)$, and find that it exhibits the following properties: 1) a steep rise towards small velocity lags (small-scales) resulting from the clumpy small-scale structure of the pre-reionization IGM, 2) a conspicuous peak at a $\Delta v_{\text{MgII}} = 768 \text{ km s}^{-1}$ arising from the doublet nature of the MgII transition, 3) a power-law shape at intermediate to large velocity lags induced by the topology of neutral regions during reionization, which is highly sensitive to their volume averaged filling fraction $\langle x_{\text{HI}} \rangle$, 4) an overall amplitude which scales as the square of the Mg abundance $[\text{Mg}/\text{H}]$.

We perform statistical inference for a correlation measurement based on a realistic mock dataset of 10 JWST

spectra and find that one can simultaneously determine the Mg abundance $[\text{Mg}/\text{H}]$, with a 1σ precision of 0.02 dex and measure the global neutral fraction $\langle x_{\text{HI}} \rangle$ to 5%, for a fiducial model with $\langle x_{\text{HI}} \rangle = 0.74$, and $[\text{Mg}/\text{H}] = -3.7$. Contrary to the naive expectation that this enrichment level, $[\text{Mg}/\text{H}]$, should be degenerate with the global neutral fraction, $\langle x_{\text{HI}} \rangle$, we find that they can be uniquely constrained owing to the distinct dependence of the correlation function shape on each parameter. Alternatively, if the IGM is pristine, then a null-detection of the MgII forest would place a stringent upper limit on the metallicity of the pre-reionization IGM of $[\text{Mg}/\text{H}] < -4.4$ at 95% credibility, assuming an independent constraints on $\langle x_{\text{HI}} \rangle > 0.5$ from another reionization probe.

We investigated the degree to which concentrations of metals in the CGM around galaxies could potentially contaminate a MgII forest signal arising from the IGM. CGM absorbers with a line density and equivalent width distribution consistent with current observational constraints were injected into our mock spectra. We analyzed the flux PDF for the models of interest, and find that the PDF for IGM absorption exhibits a broad peak around $1 - F \approx 0.01$, and a sharp exponential cutoff for $1 - F$ fluctuations a factor of a few larger. In contrast, CGM absorbers give rise to a flat flux PDF producing one to two orders of magnitude lower probability at the $1 - F$ where the IGM flux PDF peaks, but overwhelmingly dominates the absorption statistics at the larger $1 - F$ where IGM fluctuations are exponentially suppressed. Exploiting the distinct shapes of the flux PDF for IGM and CGM absorption, we present a strategy for masking the CGM contamination, and show that the difference between the correlation function $\xi(\Delta v)$ recovered from masked data and the uncontaminated IGM correlation function is negligible compared to the statistical errors.

Low frequency radio observations of the 21cm line have been touted as the premier probe of reionization because of their potential to measure $x_{\text{HI}}(z)$ and characterize the topology of reionization (see e.g. Pritchard & Loeb 2012). Our analysis illustrates that the MgII forest has tremendous potential to constrain reionization if the pre-reionization IGM is significantly enriched, so it is interesting to compare and contrast the two probes of the EoR. A rapidly developing area of 21cm cosmology are interferometric measurements with arrays like HERA (DeBoer et al. 2017) and LOFAR (van Haarlem et al. 2013) which hope to map fluctuations in 21cm emission during the EoR. These studies aim to constrain reionization by measuring the 3D 21cm emission power spectrum, whose amplitude and shape depends on the timing and topology of reionization (Madau et al. 1997; Furlanetto et al. 2006; Barkana 2009). Our approach to the MgII forest is very similar in spirit to these 21cm studies. We can also constrain the timing and topology of reionization by measuring a clustering signal, in our case the 1D correlation function of MgII absorption toward quasar sightlines. The primary disadvantage of the MgII forest is that it probes a metal line, not a primordial transition, and it is unknown whether the pre-reionization IGM is enriched. Of course given the major challenge facing all 21cm experiments – that of teasing out a miniscule signal buried beneath foregrounds and instrumental systematics that are five orders of magnitude larger (Cheng et al. 2018) – they have yet to deliver competitive constraints on the Universe’s reionization history (Mertens et al. 2020; Trott et al. 2020). In contrast,

detecting the Mg II forest in absorption is far simpler from a technical perspective, since the noise arising from the sky background and detector read noise is white, and systematics are expected to be negligible.

Of course, the most direct 21cm analog of the Mg II forest is the so-called 21cm forest, which is the prospect of observing neutral hydrogen in 21cm absorption toward a bright background radio source (Furlanetto 2006a; Carilli et al. 2002; Ciardi et al. 2013). This technique has not yet yielded any constraints owing to both the limited sensitivity of current instrumentation and the lack of sufficiently bright radio sources residing in the EoR. A significant concern is the extremely low expected 21cm optical depth,

$$\tau_{21\text{cm}} = 0.002 \left(\frac{x_{\text{HI}}}{1.0} \right) \left(\frac{T_S}{100 \text{ K}} \right)^{-1} \left(\frac{1+z}{8.5} \right)^{3/2}, \quad (24)$$

which can be directly compared to that for Mg II in eqn. (7). While the enrichment level of the pre-reionization IGM is unknown and could be extremely small, the 21cm spin temperature T_S , determined by the temperature of the pre-reionization IGM, is also highly uncertain. Indeed, the vast majority of models of early IGM thermal evolution predict that a metagalactic X-ray background sourced by early black holes photoelectrically heated the IGM to $T_S \sim 1000 \text{ K}$ (e.g. Furlanetto 2006b, but see Fialkov et al. (2014)). It is thus most likely that the 21cm forest optical depth is $\tau_{21\text{cm}} \simeq 2 \times 10^{-4}$ which will be exceedingly difficult to detect. This comparison highlights the identical dependencies of the 21cm forest and Mg II forest optical depths. The metallicity Z can be simply substituted with inverse spin temperature T_S^{-1} , and hence a spin temperature of $T_S \simeq 1000 \text{ K}$ gives the same optical depth in hydrogen as $Z/\simeq 10^{-5} Z_\odot$ would for Mg. This analogy between the 21cm forest and the Mg II forest is essentially perfect¹⁰, and the formalism, modeling, and inference procedure we have developed here can be directly applied to the 21cm forest, which will be a subject of a future paper (see also Thyagarajan 2020).

The foregoing discussion further highlights that the Achilles' heel of the Mg II forest technique is the unknown enrichment level of the pre-reionization IGM. Theory has yet to provide much guidance on this question because cosmological hydrodynamical simulations that track enrichment and properly model reionization via radiative transfer are extremely challenging, and thus only a handful of studies have addressed this question to date (Oppenheimer et al. 2009; Pallottini et al. 2014; Jaacks et al. 2018, 2019; Doughty & Finlator 2019). We opted for an extremely simplistic model of a uniformly enriched IGM for the sensitivity analyses performed here, but our correlation function approach can be easily generalized to accommodate more complex distributions of metals and/or applied directly to hydrodynamical simulations.

Indeed, empirical constraints are likely to provide the first answers to the question of early IGM enrichment. Most obvious would be a lack of detection of the Mg II forest towards quasars at sufficiently high-redshift that the IGM is known to be highly neutral, which we argued would yield

a 95% upper limit of $[\text{Mg}/\text{H}] < -4.4$ for our fiducial JWST dataset. A complementary approach would be to measure the enrichment level of the *ionized* IGM as a function of redshift approaching the EoR, using ions like C IV or Si IV. To date the highest redshift IGM metallicity measurement comes from Simcoe (2011) who measured $\text{C}/\text{H} \simeq -3.55$ at $z \sim 4.3$ via Voigt profile fitting of C IV absorbers. As previously discussed, at higher redshifts $4.5 < z < 7$, both the reduction in sensitivity as transitions redshift into the near-IR, as well as the rapidly increasing Ly α forest opacity render the line-fitting of individual absorbers hopeless. But a fruitful direction for progress would be to apply the correlation function techniques presented here to these intermediate redshift forests of absorbers in the ionized IGM, both for metal-metal auto-correlations and metal-hydrogen cross-correlations. Such auto and cross correlation measurements would enable IGM metallicity measurements in the critical $z \sim 5 - 6$ window after reionization. By comparing the clustering of high-ionization lines (e.g. C IV and Si IV) to low-ionization lines (e.g. Mg II, O I, Si II, C II) through the EoR, one could observe the high-ionization lines disappear as the low-ionization lines appear, providing the smoking-gun for the phase transition. Interpreting these metal-line forests for bluer transitions than Mg II will be more complicated, because of foreground metal-line contamination, which is why we have initially focused on Mg II. But similar to the approach adopted for the Ly α forest (McDonald et al. 2006; Palanque-Delabrouille et al. 2015) foreground metal-line contamination can be quantified using lower redshift quasars (Blomqvist et al. 2018) and statistically subtracted. This would open up the possibility of characterizing the clustering of a host of different metal absorption lines, and might even enable a measurement of relative abundance patterns in the high-redshift IGM prior to reionization, which could shed light on Pop III enrichment (Kulkarni et al. 2013, 2014).

In this study we assumed a mock dataset of 10 JWST spectra with FWHM = 100 km s⁻¹ and S/N = 100 probing the redshift range $z = 6.9 - 7.5$. At present, there are five $z > 7$ quasars known bright enough $m_{1450} \sim 20.5$ for this experiment, including two at $z > 7.5$ (Mortlock et al. 2011; Wang et al. 2018; Yang et al. 2019; Bañados et al. 2018; Yang et al. 2020). Four¹¹ of them exhibit compelling evidence for an IGM damping wing indicating that a significantly neutral IGM lies in the foreground of these quasars (Mortlock et al. 2011; Greig et al. 2017; Bañados et al. 2018; Davies et al. 2018b; Greig et al. 2019; Wang et al. 2020; Yang et al. 2020). While the full set of 10 $z > 7.5$ quasars does not yet exist, Euclid will discover over 100 quasars with $7.0 < z < 7.5$, and ~ 25 quasars beyond the current record of $z = 7.5$, including ~ 8 beyond $z = 8.0$ (Euclid et al. 2019). The brightest of these will provide the ideal targets for searching for the Mg II forest with JWST, enabling a new powerful probe of the reionization and enrichment history of the Universe.

ACKNOWLEDGEMENTS

We acknowledge helpful conversations with the ENIGMA group at UC Santa Barbara. JFH acknowledges support

¹⁰ The only differences arise from the different amounts of thermal broadening because the atomic weight of Mg is 24 times that of hydrogen (see eqn. 8)

¹¹ The fifth J0038–1527 is a broad absorption line quasar, which precludes using it to measure an IGM damping wing.

from the National Science Foundation under Grant No. 1816006. FW acknowledge the support provided by NASA through the NASA Hubble Fellowship grant #HST-HF2-51448.001-A awarded by the Space Telescope Science Institute, which is operated by the Association of Universities for Research in Astronomy, Incorporated, under NASA contract NAS5-26555. We are grateful to PRACE for awarding us access to JUWELS hosted by GCS@FZJ, Germany.

REFERENCES

- Adelberger K. L., Steidel C. C., Shapley A. E., Pettini M., 2003, *ApJ*, 584, 45
- Adelberger K. L., Shapley A. E., Steidel C. C., Pettini M., Erb D. K., Reddy N. A., 2005, *ApJ*, 629, 636
- Aguirre A., Schaye J., Kim T.-S., Theuns T., Rauch M., Sargent W. L. W., 2004, *The Astrophysical Journal*, 602, 38
- Aguirre A., Dow-Hygelund C., Schaye J., Theuns T., 2008, *The Astrophysical Journal*, 689, 851
- Almgren A. S., Bell J. B., Lijewski M. J., Lukić Z., Van Andel E., 2013, *ApJ*, 765, 39
- Asplund M., Grevesse N., Sauval A. J., Scott P., 2009, *ARA&A*, 47, 481
- Bañados E., et al., 2018, *Nature*, 553, 473
- Barkana R., 2009, *MNRAS*, 397, 1454
- Becker G. D., Sargent W. L. W., Rauch M., Simcoe R. A., 2006, *The Astrophysical Journal*, 640, 69
- Becker G. D., Rauch M., Sargent W. L. W., 2009, *The Astrophysical Journal*, 698, 1010
- Becker G. D., Sargent W. L. W., Rauch M., Calverley A. P., 2011, *The Astrophysical Journal*, 735, 93
- Becker G. D., Hewett P. C., Worseck G., Prochaska J. X., 2013, *MNRAS*, 430, 2067
- Becker G. D., et al., 2019, arXiv e-prints, p. arXiv:1907.02983
- Bergeron J., Aracil B., Petitjean P., Pichon C., 2002, *Astronomy and Astrophysics*, 396, L11
- Blomqvist M., et al., 2018, *Journal of Cosmology and Astroparticle Physics*, 2018, 029
- Boksenberg A., Sargent W. L. W., 2015, *ApJS*, 218, 7
- Booth C. M., Schaye J., Delgado J. D., Dalla Vecchia C., 2012, *MNRAS*, 420, 1053
- Bosman S. E. I., Becker G. D., Haehnelt M. G., Hewett P. C., McMahon R. G., Mortlock D. J., Simpson C., Venemans B. P., 2017, *MNRAS*, 470, 1919
- Bouché N., Murphy M. T., Péroux C., Csabai I., Wild V., 2006, *MNRAS*, 371, 495
- Busca N. G., et al., 2013, *Astronomy and Astrophysics*, 552, A96
- Calverley A. P., Becker G. D., Haehnelt M. G., Bolton J. S., 2011, *MNRAS*, 412, 2543
- Carilli C. L., Gnedin N. Y., Owen F., 2002, *ApJ*, 577, 22
- Chen S.-F. S., et al., 2017, *The Astrophysical Journal*, 850, 188
- Cheng C., et al., 2018, *ApJ*, 868, 26
- Churchill C. W., Vogt S. S., 2001, *AJ*, 122, 679
- Churchill C. W., Rigby J. R., Charlton J. C., Vogt S. S., 1999, *ApJS*, 120, 51
- Churchill C. W., Vogt S. S., Charlton J. C., 2003, *AJ*, 125, 98
- Ciardi B., et al., 2013, *MNRAS*, 428, 1755
- Coc A., Uzan J.-P., Vangioni E., 2014, *J. Cosmology Astropart. Phys.*, 2014, 050
- Cooke R. J., Pettini M., Steidel C. C., 2017, *MNRAS*, 467, 802
- Coppolani F., Petitjean P., Stoehr F., et al., 2006, *MNRAS*, 370, 1804
- Crighton N. H. M., O’Meara J. M., Murphy M. T., 2016, *MNRAS*, 457, L44
- D’Aloisio A., McQuinn M., Davies F. B., Furlanetto S. R., 2018, *MNRAS*, 473, 560
- D’Aloisio A., McQuinn M., Trac H., Cain C., Mesinger A., 2020, arXiv e-prints, p. arXiv:2002.02467
- D’Odorico V., Calura F., Cristiani S., Viel M., 2010, *MNRAS*, 401, 2715
- D’Odorico V., et al., 2013, *Monthly Notices of the Royal Astronomical Society*, 435, 1198
- D’Odorico V., et al., 2016, *MNRAS*, 463, 2690
- Davies F. B., Furlanetto S. R., 2016, *MNRAS*, 460, 1328
- Davies F. B., Hennawi J. F., 2020, in prep
- Davies F. B., Hennawi J. F., Eilers A.-C., Lukić Z., 2018a, *ApJ*, 855, 106
- Davies F. B., et al., 2018b, *ApJ*, 864, 142
- DeBoer D. R., et al., 2017, *PASP*, 129, 045001
- Doughty C., Finlator K., 2019, *MNRAS*, p. 2245
- Ellison S. L., Songaila A., Schaye J., Pettini M., 2000, *The Astronomical Journal*, 120, 1175
- Euclid et al., 2019, arXiv e-prints, p. arXiv:1908.04310
- Ferland G. J., et al., 2017, *Rev. Mex. Astron. Astrofis.*, 53, 385
- Ferrara A., 2016, in Mesinger A., ed., *Astrophysics and Space Science Library Vol. 423, Understanding the Epoch of Cosmic Reionization: Challenges and Progress.* p. 163 (arXiv:1511.01120), doi:10.1007/978-3-319-21957-8_6
- Fialkov A., Barkana R., Visbal E., 2014, *Nature*, 506, 197
- Frebel A., Norris J. E., 2015, *ARA&A*, 53, 631
- Fumagalli M., O’Meara J. M., Prochaska J. X., 2011, *Science*, 334, 1245
- Fumagalli M., O’Meara J. M., Prochaska J. X., 2016, *MNRAS*, 455, 4100
- Furlanetto S. R., 2006a, *MNRAS*, 370, 1867
- Furlanetto S. R., 2006b, *MNRAS*, 371, 867
- Furlanetto S. R., Oh S. P., Briggs F. H., 2006, *Phys. Rep.*, 433, 181
- Gauthier J.-R., Chen H.-W., Cooksey K. L., Simcoe R. A., Seyfert E. N., O’Meara J. M., 2014, *MNRAS*, 439, 342
- Gnedin N. Y., Hui L., 1998, *MNRAS*, 296, 44
- Gnedin N. Y., Ostriker J. P., 1997, *The Astrophysical Journal*, 486, 581
- Greig B., Mesinger A., Haiman Z., Simcoe R. A., 2017, *MNRAS*, 466, 4239
- Greig B., Mesinger A., Bañados E., 2019, *MNRAS*, 484, 5094
- Haardt F., Madau P., 2012, *ApJ*, 746, 125
- Hahn O., Abel T., 2011, *MNRAS*, 415, 2101
- Hoag A., et al., 2019, *ApJ*, 878, 12
- Howlett C., Lewis A., Hall A., Challinor A., 2012, *J. Cosmology Astropart. Phys.*, 2012, 027
- Iršič V., et al., 2017, *Phys. Rev. D*, 96, 023522
- Jaacks J., Thompson R., Finkelstein S. L., Bromm V., 2018, *MNRAS*, 475, 4396
- Jaacks J., Finkelstein S. L., Bromm V., 2019, *MNRAS*, 488, 2202
- Kacprzak G. G., Churchill C. W., 2011, *ApJ*, 743, L34
- Keating L. C., Haehnelt M. G., Becker G. D., Bolton J. S., 2014, *Monthly Notices of the Royal Astronomical Society*, 438, 1820
- Keating L. C., Weinberger L. H., Kulkarni G., Haehnelt M. G., Chardin J., Aubert D., 2020, *MNRAS*, 491, 1736
- Kirihara T., Hasegawa K., Umemura M., Mori M., Ishiyama T., 2020, *MNRAS*, 491, 4387
- Kulkarni G., Rollinde E., Hennawi J. F., Vangioni E., 2013, *ApJ*, 772, 93
- Kulkarni G., Hennawi J. F., Rollinde E., Vangioni E., 2014, *ApJ*, 787, 64
- Kulkarni G., Hennawi J. F., Oñorbe J., Rorai A., Springel V., 2015, *ApJ*, 812, 30
- Kulkarni G., Keating L. C., Haehnelt M. G., Bosman S. E. I., Puchwein E., Chardin J., Aubert D., 2019, *MNRAS*, 485, L24
- Lacey C., Cole S., 1993, *MNRAS*, 262, 627
- Lee K.-G., et al., 2015, *The Astrophysical Journal*, 799, 196
- Lewis A., Challinor A., Lasenby A., 2000, *ApJ*, 538, 473

- Lukić Z., Stark C. W., Nugent P., White M., Meiksin A. A., Almgren A., 2015, *MNRAS*, 446, 3697
- Lundgren B. F., et al., 2009, *ApJ*, 698, 819
- Madau P., Fragos T., 2017, *ApJ*, 840, 39
- Madau P., Shull J. M., 1996, *The Astrophysical Journal*, 457, 551
- Madau P., Meiksin A., Rees M. J., 1997, *ApJ*, 475, 429
- Madau P., Ferrara A., Rees M. J., 2001, *The Astrophysical Journal*, 555, 92
- Madau P., Rees M. J., Volonteri M., Haardt F., Oh S. P., 2004, *ApJ*, 604, 484
- Martin C. L., Scannapieco E., Ellison S. L., Hennawi J. F., Djorgovski S. G., Fournier A. P., 2010, *ApJ*, 721, 174
- Mas-Ribas L., Riemer-Sørensen S., Hennawi J. F., Miralda-Escudé J., O’Meara J. M., Pérez-Ràfols I., Murphy M. T., Webb J. K., 2018, *ApJ*, 862, 50
- Mason C. A., Treu T., Dijkstra M., Mesinger A., Trenti M., Pentericci L., de Barros S., Vanzella E., 2018, *ApJ*, 856, 2
- Mason C. A., et al., 2019, *MNRAS*, 485, 3947
- Mathes N. L., Churchill C. W., Murphy M. T., 2017, arXiv e-prints, p. arXiv:1701.05624
- McDonald P., Miralda-Escudé J., Rauch M., Sargent W. L. W., Barlow T. A., Cen R., 2001, *The Astrophysical Journal*, 562, 52
- McDonald P., Seljak U., Cen R., Bode P., Ostriker J. P., 2005a, *Monthly Notices of the Royal Astronomical Society*, 360, 1471
- McDonald P., et al., 2005b, *The Astrophysical Journal*, 635, 761
- McDonald P., et al., 2006, *The Astrophysical Journal Supplement Series*, 163, 80
- Mertens F. G., et al., 2020, *MNRAS*, 493, 1662
- Mesinger A., Furlanetto S., Cen R., 2011, *MNRAS*, 411, 955
- Miralda-Escudé J., Rees M. J., 1997, *The Astrophysical Journal*, 478, L57
- Mortlock D. J., et al., 2011, *Nature*, 474, 616
- Narayanan A., Misawa T., Charlton J. C., Kim T.-S., 2007, *ApJ*, 660, 1093
- Nasir F., D’Aloisio A., 2020, *MNRAS*, 494, 3080
- Nestor D. B., Turnshek D. A., Rao S. M., 2005, *ApJ*, 628, 637
- Oñorbe J., Hennawi J. F., Lukić Z., 2017, *ApJ*, 837, 106
- Oñorbe J., Davies F. B., Lukić Z., Hennawi J. F., Sorini D., 2019, *MNRAS*, 486, 4075
- Oh S. P., 2002, *Monthly Notices of the Royal Astronomical Society*, 336, 1021
- Oppenheimer B. D., Davé R., Finlator K., 2009, *Monthly Notices of the Royal Astronomical Society*, 396, 729
- Palanque-Delabrouille N., et al., 2015, *Journal of Cosmology and Astro-Particle Physics*, 2015, 011
- Pallottini A., Ferrara A., Gallerani S., Salvadori S., D’Oro V., 2014, *Monthly Notices of the Royal Astronomical Society*, 440, 2498
- Pawlik A. H., Rahmati A., Schaye J., Jeon M., Dalla Vecchia C., 2017, *MNRAS*, 466, 960
- Petitjean P., Bergeron J., 1990, *A&A*, 231, 309
- Petitjean P., Bergeron J., 1994, *A&A*, 283, 759
- Pichon C., Scannapieco E., Aracil B., Petitjean P., Aubert D., Bergeron J., Colombi S., 2003, *ApJ*, 597, L97
- Pieri M. M., 2014, *Monthly Notices of the Royal Astronomical Society*, 445, L104
- Planck et al., 2018, arXiv e-prints, p. arXiv:1807.06209
- Pritchard J. R., Loeb A., 2012, *Reports on Progress in Physics*, 75, 086901
- Prochaska J. X., et al., 2013, *ApJ*, 776, 136
- Quashnock J. M., Stein M. L., 1999, *ApJ*, 515, 506
- Quashnock J. M., Vanden Berk D. E., 1998, *ApJ*, 500, 28
- Rauch M., Sargent W. L. W., Womble D. S., Barlow T. A., 1996, *ApJ*, 467, L5
- Ricotti M., Ostriker J. P., 2004, *Monthly Notices of the Royal Astronomical Society*, 350, 539
- Robert P. F., Murphy M. T., O’Meara J. M., Crighton N. H. M., Fumagalli M., 2019, *MNRAS*, 483, 2736
- Rogers K. K., Bird S., Peiris H. V., Pontzen A., Font-Ribera A., Leistedt B., 2018, *MNRAS*, 474, 3032
- Rorai A., et al., 2017, *Science*, 356, 418
- Ryan-Weber E. V., Pettini M., Madau P., Zych B. J., 2009, *Monthly Notices of the Royal Astronomical Society*, 395, 1476
- Sargent W. L. W., Young P. J., Boksenberg A., Tytler D., 1980, *ApJS*, 42, 41
- Sargent W. L. W., Boksenberg A., Steidel C. C., 1988, *ApJS*, 68, 539
- Scannapieco E., Pichon C., Aracil B., Petitjean P., Thacker R. J., Pogosyan D., Bergeron J., Couchman H. M. P., 2006, *MNRAS*, 365, 615
- Schaye J., Aguirre A., Kim T.-S., Theuns T., Rauch M., Sargent W. L. W., 2003, *The Astrophysical Journal*, 596, 768
- Schechter P., 1976, *ApJ*, 203, 297
- Seljak U., McDonald P., Makarov A., 2003, *Monthly Notices of the Royal Astronomical Society*, 342, L79
- Simcoe R. A., 2011, *The Astrophysical Journal*, 738, 159
- Simcoe R. A., et al., 2011, *The Astrophysical Journal*, 743, 21
- Simcoe R. A., Sullivan P. W., Cooksey K. L., Kao M. M., Matejsek M. S., Burgasser A. J., 2012, *Nature*, 492, 79
- Slosar A., et al., 2013, *Journal of Cosmology and Astro-Particle Physics*, 2013, 026
- Songaila A., 2005, *AJ*, 130, 1996
- Steidel C. C., Sargent W. L. W., 1992, *ApJS*, 80, 1
- Thyagarajan N., 2020, arXiv e-prints, p. arXiv:2006.10070
- Trott C. M., et al., 2020, *MNRAS*, 493, 4711
- Tytler D., et al., 2009, *MNRAS*, 392, 1539
- Viel M., Becker G. D., Bolton J. S., Haehnelt M. G., 2013, *Phys. Rev. D*, 88, 043502
- Vikas S., et al., 2013, *ApJ*, 768, 38
- Walther M., Hennawi J. F., Hiss H., Oñorbe J., Lee K.-G., Rorai A., O’Meara J., 2018, *ApJ*, 852, 22
- Walther M., Oñorbe J., Hennawi J. F., Lukić Z., 2019, *The Astrophysical Journal*, 872, 13
- Wang F., et al., 2018, *ApJ*, 869, L9
- Wang F., et al., 2020, *ApJ*, 896, 23
- Wyithe J. S. B., Bolton J. S., 2011, *MNRAS*, 412, 1926
- Xu H., Ahn K., Norman M. L., Wise J. H., O’Shea B. W., 2016, *ApJ*, 832, L5
- Yang J., et al., 2019, *AJ*, 157, 236
- Yang J., et al., 2020, *ApJ*, 897, L14
- Zel’Dovich Y. B., 1970, *A&A*, 500, 13
- Zhu G., Ménard B., 2013, *The Astrophysical Journal*, 773, 16
- du Mas des Bourboux H., et al., 2019, *The Astrophysical Journal*, 878, 47
- van Haarlem M. P., et al., 2013, *A&A*, 556, A2

This paper has been typeset from a $\text{\TeX}/\text{\LaTeX}$ file prepared by the author.